Title	Nongyrotropic electron velocity distribution functions near the lunar surface
Author(s)	Harada, Yuki; Machida, Shinobu; Saito, Yoshifumi; Yokota, Shoichiro; Asamura, Kazushi; Nishino, Masaki N.; Tsunakawa, Hideo; Shibuya, Hidetoshi; Takahashi, Futoshi; Matsushima, Masaki; Shimizu, Hisayoshi
Citation	Journal of Geophysical Research (2012), 117
Issue Date	2012-07-20
URL	http://hdl.handle.net/2433/160049
Right	©2012. American Geophysical Union.
Type	Journal Article
Textversion	author

Nongyrotropic Electron Velocity Distribution Functions near the Lunar Surface

Yuki Harada,[1] Shinobu Machida,[1] Yoshifumi Saito,[2] Shoichiro Yokota,[2] Kazushi Asamura,[2] Masaki N. Nishino,[2] Hideo Tsunakawa,[3] Hidetoshi Shibuya,[4] Futoshi Takahashi,[3] Masaki Matsushima,[3] and Hisayoshi Shimizu[5]

K. Asamura, M. N. Nishino, Y. Saito and S. Yokota, Institute of Space and Astronautical Science, Japan Aerospace Exploration Agency, 3-1-1 Yoshinodai, Chuo-ku, Sagamihara 252-5210, Japan.

Y. Harada and S. Machida, Department of Geophysics, Kyoto University, Oiwake-cho, Sakyo-ku, Kyoto 606-8502, Japan. (haraday@kugi.kyoto-u.ac.jp)

M. Matsushima, F. Takahashi and H. Tsunakawa, Department of Earth and Planetary Sciences, Tokyo Institute of Technology, 2-12-1 Ookayama, Tokyo 152-8551, Japan.

H. Shibuya, Department of Earth and Environmental Sciences, Kumamoto University, Kumamoto 860-8555, Japan.

H. Shimizu, Earthquake Research Institute, University of Tokyo, 1-1-1 Yayoi, Tokyo 113-0032, Japan.

[1]Department of Geophysics, Kyoto

Abstract.

We have analyzed nongyrotropic electron velocity distribution functions (VDFs) obtained near the lunar surface. Electron VDFs, measured at ∼10–100 km altitude by Kaguya in both the solar wind and the Earth's magnetosphere, exhibit nongyrotropic empty regions associated with the 'gyro-loss' effect; i.e., electron absorption by the lunar surface combined with electron gyromotion. Particle-trace calculations allow us to derive theoretical forbidden regions in the electron VDFs, thereby taking into account the modifications due to nonuniform magnetic fields caused by diamagnetic-current sys-

University, Kyoto, Japan.

[2]Institute of Space and Astronautical Science, Japan Aerospace Exploration Agency, Sagamihara, Japan.

[3]Department of Earth and Planetary Sciences, Tokyo Institute of Technology, Tokyo, Japan.

[4]Department of Earth and Environmental Sciences, Kumamoto University, Kumamoto, Japan.

[5]Earthquake Research Institute, University of Tokyo, Tokyo, Japan.

tems, lunar-surface charging, and electric fields perpendicular to the magnetic field. Comparison between the observed empty regions with the theoretically derived forbidden regions suggests that various components modify the characteristics of the nongyrotropic electron VDFs depending on the ambient-plasma conditions. On the lunar nightside in the magnetotail lobes, negative surface potentials slightly reduce the size of the forbidden regions, but there are no distinct effects of either the diamagnetic current or perpendicular electric fields. On the dayside in the solar wind, the observations suggest the presence of either the diamagnetic-current or solar-wind convection electric-field effects, or both. In the terrestrial plasma sheet, all three mechanisms can substantially modify the characteristics of the forbidden regions. The observations imply the presence of a local electric field of at least 5 mV/m although the mechanism responsible for production of such a strong electric field is unknown. Analysis of nongyrotropic VDFs associated with the gyroloss effect near solid surfaces can promote a better understanding of the near-surface plasma environment and of plasma–solid-surface interactions.

1. Introduction

The Moon orbits the Earth with an orbital radius of $\sim 60R_{\mathrm{E}}$ ($1R_{\mathrm{E}} = 6378$ km). Along its way, it passes through various regions, including the solar wind, the terrestrial magnetosheath, the magnetotail lobes, and the plasma sheet. In each of these regions, the plasma conditions near the Moon vary widely in density and energy. The various types of plasma interact directly with the lunar surface because of the lack of both a global magnetic field and a thick atmosphere. Therefore, the plasma near the Moon is suitable for investigation of the interactions of charged particles with solid surfaces. Most charged particles that strike the lunar surface will be absorbed, although there exist a small number of backscattering electrons and protons, as well as secondary electrons and ions [*Halekas et al.*, 2009a; *Saito et al.*, 2008a; *Yokota et al.*, 2009].

The lunar electromagnetic environment has been studied since plasma and magnetic fields were first measured in the 1960s and 1970s [*Schubert and Lichtenstein*, 1974]. Explorer 35 observations revealed the fundamental features of the interaction between the Moon and the solar wind. A tenuous region, called the lunar wake, is formed behind the Moon because of the absorption of solar-wind electrons and ions by the lunar surface [*Lyon et al.*, 1967]. Enhanced magnetic fields in the wake, as well as reduced fields near the wake boundary, have been observed, which can be explained in terms of diamagnetic-current systems [*Colburn et al.*, 1967]. A diamagnetic sheet current at the wake boundary, caused by the decrease in density of gyrating particles, produces a magnetic field, which increases in the central wake.

During this period, lunar shadowing techniques were used to infer magnetospheric convection electric fields at the Moon's distance [*Anderson*, 1970]. The presence of convection electric fields can be deduced through detection of the $\mathbf{E} \times \mathbf{B}$ drift displacement of low-energy electrons at the edge of the lunar electron shadow. *McCoy et al.* [1975] reported a typical value of 0.15 mV/m, spanning the range from $\sim$ 0.02 mV/m (the method's sensitivity limit) to 2 mV/m, based on analysis of particle and magnetic-field data obtained by the Apollo 15 and 16 subsatellites. They also showed that the sense of the electric field is almost always in the direction from dawn to dusk, but it is often variable both in time and space.

In the late 1990s, three-dimensional (3D) measurements of low-energy electrons and magnetic fields were conducted by the Lunar Prospector. These observations revealed electrons that were reflected by both electric and magnetic fields, indicating that the lunar surface is negatively charged [*Halekas et al.*, 2002]. Electrostatic potentials of the lunar surface as large as -1 kV were observed in the plasma sheet, and large potentials of up to -4.5 kV were found during solar energetic-particle events [*Halekas et al.*, 2008, 2009b]. The lunar surface potential varies from sunlight to shadow and depends on the ambient-plasma conditions.

Although ions and electrons are usually expected to have gyrotropic (i.e., symmetric relative to the magnetic-field lines) velocity distribution functions (VDFs) in the plasma's rest frame, they can form nongyrotropic VDFs due to shocks, boundaries, or waves. Three possible mechanisms to generate nongyrotropic (gyrophase-bunched) ions include (i) a pick-up process of ions by the solar wind, (ii) plasma inhomogeneities on spatial scales smaller than the ion gyroradius, and (iii) wave–particle interactions (resonant trapping by waves). Nongyrotropic ions thought to have been produced by these mechanisms have been widely observed near the Earth's bow shock and interplanetary shocks, in the current sheet and the plasma-sheet boundary layer in the Earth's magnetotail, and near comets, planets, the Moon, and in similar environments [*Meziane et al.*, 1999; *Armstrong et al.*, 1992; *Tu et al.*, 1997; *Mukai et al.*, 1998; *Coates and Jones*, 2009; *Futaana et al.*, 2003].

In contrast to the large number of observations of nongyrotropic *ion* VDFs, only a few observational papers exist that focus on nongyrotropic *electron* VDFs. The small electron gyroradius and short gyroperiod compared with the ion gyroradius and gyroperiod cause great difficultly in attempts to detect nongyrotropic electron VDFs [*Leubner*, 2003]. Some signatures of a gyrophase-bunched electron VDF were observed just upstream of the Earth's bow shock, first by ISEE 1 and ISEE 2, and subsequently by WIND [*Anderson et al.*, 1985; *Gurgiolo et al.*, 2000]. Although a local phase-trapping distribution is thought to be necessary for gyrophase-bunched electron observations, the mechanism responsible for producing these nongyrotropic electrons is as yet unknown.

A recent analysis of high-angular-resolution data of low-energy electrons, as well as of magnetic-field data obtained by Kaguya (SELENE), revealed a partial loss in the electron VDF caused by the 'gyro-loss' effect [*Harada et al.*, 2010]. Electron VDFs produced by this effect are nongyrotropic. They exhibit energy-dependent empty regions for certain gyrophases. One of the observed electron VDFs suggests the presence of a relatively strong electric field (~ 10 mV/m) near the Moon when it is located in the plasma sheet. However, it remains uncertain whether this electron VDF was formed only because of the electric field.

The gyro-loss effect is essentially the same as 'cyclotron shadowing' considered in the Apollo era. *McGuire* [1972] first theoretically treated shadowing of gyrating particles by an absorbing surface and calculated the reduction in omnidirectional particle flux observed by lunar orbiters. *Reiff* [1976a] investigated how cyclotron shadowing affects the observation of ions and electrons by a detector on the lunar surface, analytically and numerically calculating the 'shadow zones', namely the magnetic-field directions for which particles are not observable by a given look direction of a lunar-based detector. In addition to cyclotron motion of electrons, *Reiff and Burke* [1976b] took the local crustal magnetic field at the Apollo 14 site into account in their numerical calculations. They showed that their calculations were consistent with a 'magnetic shadowing' observation of plasma sheet electrons by CPLEE, which consists of two small-aperture detectors. Kaguya's high-angular-resolution measurement of 3D electron VDF provides us clear observational evidence of cyclotron shadowing in low lunar orbits.

This paper presents further theoretical considerations of the gyro-loss effect on electron VDFs based on particle-trace calculations and additional analysis of the data obtained by Kaguya. In our previous work, only the ideal and simple case of a uniform magnetic field parallel to a plane surface was considered. Test-particle tracing allows us to take into account more realistic and complicated configurations, including the spherical lunar surface, inclined and nonuniform magnetic fields, the negatively charged lunar surface, electric fields, etc. We mainly discuss the interaction between electrons and the lunar surface, which has a scale length that is characterized by the electron gyrodiameter and that produces nongyrotropic electron VDFs.

2. Instrumentation and Coordinates

We use data obtained by the MAP (MAgnetic field and Plasma experiment) instrument on Kaguya, which consists of two components: LMAG (Lunar MAGnetometer) and PACE (Plasma energy Angle and Composition Experiment). LMAG is a triaxial fluxgate magnetometer, which is used to observe the magnetic field with a sampling frequency of 32 Hz and a resolution of 0.1 nT [*Shimizu et al.*, 2008; *Takahashi et al.*, 2009; *Tsunakawa et al.*, 2010]. We use 1 s magnetic-field data in the present study. Low-energy charged particles near the Moon are observed by PACE, which consists of four sensors: two electron spectrum analyzers (ESA-S1 and ESA-S2), an ion mass analyzer (IMA), and an ion energy analyzer (IEA) [*Saito et al.*, 2008b, 2010]. ESA-S1 and ESA-S2 measure the distribution functions of low-energy electrons in the energy ranges of 6 eV–9 keV and 9 eV–16 keV, respectively. Each electron sensor has a hemispherical field of view, with angular resolutions of 5° in elevation and 8° in azimuthal angle (FWHM). We use the satellite coordinates; i.e., $+Z$ is directed towards the lunar surface, $+X$ or $-X$ is the direction of travel, and Y completes the orthogonal coordinate set (see Figures 1a and 1d). We define the azimuthal angle of the magnetic field in the satellite coordinates as ϕ_{Bsat} and the corresponding elevation angle as θ_{Bsat}.

3. Gyro-loss Effect on Electron Velocity Distribution Functions

3.1. Theoretical Predictions Based on Particle-Trace Calculations

A charged particle gyrates around magnetic-field lines with a gyroradius (Larmor radius) given by $r_{\mathrm{L}} = mv_{\perp}/|q|B$, where m is the particle mass, $v_{\perp}$ the velocity component perpendicular to the magnetic field, q the electric charge, and B the magnetic-field intensity. Consider a VDF at an altitude H in the presence of a magnetic field oriented parallel to a plane solid surface: see Figure 1a. As shown by the red dashed lines in Figure 1a, some particles on orbits with gyrodiameters greater than or equal to H strike the surface and are absorbed because of gyromotion. This absorption results in an empty region in the VDF. This gyro-loss effect is expected to be seen in electron VDFs observed by Kaguya, because the gyrodiameter of electrons near the Moon (1 keV electrons have a gyrodiameter of 107 km in a 2 nT magnetic field) is comparable in length to Kaguya's orbital height (∼10–100 km). In this paper, we refer to 'empty regions' and 'forbidden regions' when we describe features in observations and theoretical predictions, respectively, following *Harada et al.* [2010].

To consider the gyro-loss effect on electron VDFs observed by Kaguya, we perform particle-trace calculations using a fourth-order Runge–Kutta integration method. We backtrace a test electron from the spacecraft and check whether or not it strikes the lunar surface, assuming the Moon to be a sphere with a radius of $1R_{\mathrm{M}}$ ($1R_{\mathrm{M}} = 1738$ km). The black trace in Figure 1d shows an example of an electron trajectory that results in a collision with the lunar surface in the presence of a uniform magnetic field that is locally parallel to the lunar surface at the spacecraft's position ($\theta_{\mathrm{Bsat}} = 0°$) and in the absence of electric fields. We launch electrons characterized by an initial velocity distribution divided into 64 elevation angles, 64 azimuthal angles, and four different kinetic energies. This way, we derive 'forbidden regions' in the electron VDFs. Electrons launched with velocities in these forbidden regions strike the lunar surface.

For a uniform magnetic field that is locally parallel to the lunar surface at the spacecraft's locus and in the absence of electric fields, the derived forbidden regions are shown in white in Figure 2. We trace electrons with a time step of 1/50 of the gyroperiod T_{ce}

from the spacecraft's altitude of 100 km until they either strike the lunar surface or gyrate one cycle, $t \geq -T_{ce}$. (One cycle is sufficient to see whether an electron strikes the Moon in the presence of a parallel magnetic field.) In Figure 2, the high-energy forbidden regions are larger than their low-energy counterparts, since more electrons strike the lunar surface because of the larger gyroradii associated with higher energies. The forbidden regions appear at an azimuthal angle of around 90° and an elevation angle of approximately 0°. At these angles, where the guiding center of the electrons is located between the spacecraft and the lunar surface nearest the spacecraft (the bottom red circles in Figure 1a), electrons strike the lunar surface with the minimum energy.

Harada et al. [2010] showed that a critical gyroradius, r_{c}, is given for a gyrophase ψ by

$$r_{\mathrm{c}} = \frac{H}{1 - \cos\psi}, \tag{1}$$

as illustrated in Figure 1b. Electrons with $r_{\mathrm{L}} \geq r_{\mathrm{c}}$ strike the lunar surface. The dashed lines in Figure 2 indicate the forbidden regions derived from Equation (1). These regions are symmetric with respect to the (v_x, v_y) plane, since the lunar surface is assumed to be planar. By contrast, the forbidden regions derived from the particle-trace calculation (white regions in Figure 2) are asymmetric relative to the (v_x, v_y) plane since we assume the Moon to be a sphere: the time in which electrons that are launched for reverse tracking with initial z-component velocity $v_z > 0$ (the regions of positive elevation angle in Figure 2 and $180 < \psi < 360°$ in Figure 1b) gyrate from the spacecraft to the lunar surface is longer than for electrons with $v_z < 0$. Therefore, electrons with $v_z > 0$ can move long distances along the magnetic-field lines (thus increasing their effective height because of the spherical Moon) and the forbidden regions for $v_z > 0$ are smaller than those for $v_z < 0$.

For magnetic-field lines that pass through the spacecraft under an angle but do not intersect the lunar surface, the derived forbidden regions are shown in Figure 3. We perform this calculation by adopting $\theta_{\mathrm{Bsat}} = +10^\circ$ (the magnetic-field line at 100 km intersects the Moon with $\theta_{\mathrm{Bsat}} \geq +19^\circ$). We continuously trace electrons until they either strike the lunar surface or gyrate twenty cycles: $t \geq -20T_{ce}$. The dashed lines in Figure 3 indicate the regions where the electrons strike the surface during one cycle. Although the forbidden regions in Figure 3 also appear at an azimuthal angle of around 90° and an elevation angle of approximately 0°, they have different distributions from those shown in Figure 2. The forbidden regions are large for pitch angles $\alpha > 90^\circ$, since electrons gyrate upwards along the magnetic-field lines. In the forbidden regions with $\alpha > 90^\circ$, electrons launched from the spacecraft for reverse tracking can strike the lunar surface after they gyrate more than one cycle, as indicated by the orange trace in Figure 1d. On the other hand, electrons in the forbidden regions with $\alpha < 90^\circ$ strike the lunar surface in one gyrocycle, because they move away form the lunar surface during reverse tracking. Electrons with $\alpha > 90^\circ$ pass near the lunar surface and can strike with lower energies than electrons with $\alpha < 90^\circ$ if $\theta_{\mathrm{Bsat}} > 0$.

3.2. Gyro-loss Events in the Earth's Magnetosphere and the Solar Wind

Harada et al. [2010] showed the occurrence of two gyro-loss events observed at Kaguya's orbital height of more than 50 km when the Moon was located in the Earth's magnetosphere. Figure 4 shows another example, observed at an altitude of only 12 km (detailed information and time-series data are included in Table 1 and shown in Figure 5). At this time, the Moon was thought to be located in either the plasma-sheet boundary layer or the magnetotail lobe, and Kaguya was located on the nightside of the Moon near the south pole (at latitude 76°S, longitude 149°E in selenographic coordinates), where relatively weak and/or small-scale magnetic anomalies exist [*Tsunakawa et al.*, 2010]. The red solid lines in Figure 4 show the forbidden regions derived from the particle-trace calculation using the magnetometer data and assuming an inclined, uniform magnetic field without any electric fields. Empty regions clearly appeared at an azimuthal angle of around 135°. They roughly correspond to the theoretically derived forbidden regions indicated by the red solid lines, although the empty regions seem to be somewhat smaller than the forbidden regions. At lower altitudes of $\sim$ 10 km, the gyro-loss effect is clearly seen, even for lower energies of a few hundred eV.

Figure 6 shows an electron VDF observed during Event 2, when the Moon was located in the solar wind and Kaguya's position was on the far side (at latitude 36°S, longitude 104°W in selenographic coordinates), where strong magnetic anomalies do not exist [*Tsunakawa et al.*, 2010]. Detailed information and time-series data for Event 2 are included in Table 1 and shown in Figure 7. In the solar wind, the electron temperature is significantly lower than that in the terrestrial plasma sheet, and observed counts of higher-energy electrons are very small. Therefore, we did not observe the gyro-loss effect at higher altitudes and even at lower altitudes, we have to average counts over a certain interval to see the gyro-loss effect on electron VDFs in the solar wind. Figure 6 shows the electron distribution averaged during the period covering 11:57:22–11:58:42 UT on 17 April 2009, when the magnetic field was quite stable and nearly parallel to the lunar surface. The electron flux clearly decreases in the theoretically derived forbidden regions indicated by the red lines in Figure 6. This shows the gyro-loss effect on electron VDFs also when the Moon is located in the solar wind, although there are slight differences between these red lines and the boundaries of the observed empty regions.

We have shown the two gyro-loss events observed in both the Earth's magnetosphere and the solar wind. The observed electron VDFs are relatively consistent with theoretical predictions for uniform magnetic fields without electric fields. However, we also found some distributions exhibiting empty regions that do not correspond to the theoretically derived forbidden regions based on this simple assumption. Two examples that have remarkably different distributions from the simple theoretical predictions are shown in Figures 8 and 9 (detailed information and time-series data are included in Table 1 and shown in Figures 10 and 11). Both of these events were observed when Kaguya was located above the rather weak and/or small-scale crustal-field regions [*Tsunakawa et al.*, 2010], and the Moon was located in the high-temperature and weak-magnetic-field regions in the central plasma sheet. The electron VDFs of these events indicate that large numbers of electrons were observed in the forbidden regions indicated by the red lines. The electron motions and forbidden regions were thought to be greatly modified by some factors, including electric and nonuniform magnetic fields. We do not deal with the effects of lunar magnetic anomalies in this paper, although they may play an important role, in particular around strong magnetic anomalies. Nonuniform magnetic fields caused by a diamagnetic-current system near the lunar surface, lunar-surface charging, and electric fields perpendicular to the magnetic field are discussed below.

4. Diamagnetic-Current Effect

Nongyrotropic electron VDFs produced by the gyro-loss effect are related to a diamagnetic-current system formed by the pressure gradient near the lunar surface. The diamagnetic current produces magnetic fields, resulting in nonuniform magnetic-field structures. The nonuniform magnetic fields will modify the electron trajectories and, consequently, the forbidden regions. This diamagnetic-current effect will contribute strongly in the presence of high plasma pressure and weak magnetic fields. In this section, we consider how the diamagnetic-current system affects the forbidden regions in electron VDFs.

When we consider the lunar surface and a magnetic field that is parallel to the surface, high-energy, hot electrons are gradually lost as the altitude H decreases because of the gyro-loss effect, and the pressure gradient near the surface forms a diamagnetic-current system (see Figure 1a). Although numerous hot electrons are lost near the surface, charge neutrality would be preserved by field-aligned intrusion of cold electrons, which are not lost through the gyro-loss effect because of their small gyroradii.

For the ambient plasma near the Moon, most ions have gyroradii that are much larger than H or even larger than the lunar radius, except when the Moon is in the magnetotail lobes. These ions are not magnetized on the scale length considered here, and we do not take into account the ion diamagnetic current near the lunar surface.

In the presence of a gradient of perpendicular pressure to the magnetic field, $\nabla p_{e\perp}$, the diamagnetic electron current is given by

$$\mathbf{J}_{\mathrm{D}e} = \frac{\mathbf{B} \times \nabla p_{e\perp}}{B^2} = \frac{\mathbf{B} \times \nabla (n_{\mathrm{eh}} k_{\mathrm{B}} T_{\mathrm{eh}\perp})}{B^2}, \tag{2}$$

where n_{eh} and T_{eh} are the density and temperature of hot electrons, respectively, and k_{B} is the Boltzmann constant. We assume that cold electrons do not contribute to the electron perpendicular pressure; i.e., $n_{ec} k_{\mathrm{B}} T_{ec\perp} = 0$. If the magnetic field is oriented parallel to a plane solid surface ($+X$ direction), as illustrated in Figure 1a, the electron diamagnetic current flows parallel to the lunar surface ($+Y$ direction), since $\nabla p_{e\perp}$ directs away from the lunar surface ($-Z$ direction). In terms of the electron VDF, there are more electrons with negative than with positive Y velocity. These with positive Y velocity are partially lost because of the gyro-loss effect. Therefore, the $-Y$-directed bulk electron velocity, $\mathbf{V}_e$, produces an electron current, $\mathbf{J}_e$, in the $+Y$ direction.

Figure 12 shows a cross section of a modeled hot-electron VDF using the coordinate system defined in Figure 1a. We assume that the ambient electrons' velocity distribution is Maxwellian, with a density of 0.1 cm^{-3} and a temperature of 400 eV. We derive the forbidden region at an altitude of 50 km in the presence of a magnetic field of ~ 3.2 nT. We can obtain the same result, no matter whether we use Equation (1) or the particle-trace calculation, because the lunar surface is assumed to be planar while the magnetic field is assumed to be parallel to the lunar surface. The boundary of the forbidden region in the (v_y, v_z) plane becomes a parabola, as derived from Equation (1). Figure 12 shows that the bulk velocity of hot electrons $\mathbf{V}_{e\mathrm{h}}$ has a $-Y$ component because a large part of the region for $v_y > 0$ is lost. By calculating the moments of this modeled electron VDF, $n_{e\mathrm{h}}$, $\mathbf{V}_{e\mathrm{h}}$, and $\mathbf{J}_e$ can be derived.

The distribution of $n_{e\mathrm{h}}$ calculated for each altitude is shown by black lines in the top left-hand panel of Figure 13, $V_{e\mathrm{h}}$ is shown in the top right-hand panel, and J_e in the bottom left-hand panel. We calculated the moments for the energy range from -10 to $+10$ keV below an altitude of 150 km for 1 km steps. Here, $V_{e\mathrm{h}} = |V_{e\mathrm{h}y}|$ and $J_e = J_{ey}$, because the modeled electron VDF is symmetric relative to the (v_y, v_x) and (v_y, v_z) planes. The current layer with a peak at around 20 km is present below an altitude of 100 km, where the hot-electron density decreases and the corresponding velocity increases. The distribution of J_e depends on the parameters of the calculation; i.e., the ambient electron density, n_{e0}, the ambient electron temperature, T_{e0}, and the ambient magnetic-field intensity, B_0. The vertical scale length of the current layer, L, depends on the electron gyrodiameter; i.e., $L \propto \sqrt{T_{e0}}/B_0$. If we define $L \equiv 100$ km based on Figure 13, with $T_{e0} = 400$ eV and $B_0 \sim 3.2$ nT, we get

$$L \sim 16 \frac{\sqrt{T_{e0}}}{B_0} \quad \text{km}, \tag{3}$$

with T_{e0} expressed in units of eV and B_0 in nT. Since the intensity of the current $J_e \propto T_{e0} n_{e0}/B_0 L$ – Equation (2) – we obtain $J_e \propto n_{e0}\sqrt{T_{e0}}$.

The diamagnetic current produces a magnetic field that reduces the ambient magnetic field above and enhances the magnetic field below the current layer (see Figure 1a). Using Ampère's law, an infinite current sheet with a current per unit length I produces a magnetic field $B = \mu_0 I/2$. The magnetic field associated with the diamagnetic current is derived from Equation (2) as

$$B_{\mathrm{D}} = \frac{\mu_0 I}{2} = \frac{\mu_0}{2} \frac{n_{e0} k_{\mathrm{B}} T_{e0}}{B_0 L} L \sim 0.1 \frac{n_{e0} T_{e0}}{B_0} \quad \text{nT}, \tag{4}$$

with n_{e0} expressed in units of cm^{-3}, T_{e0} in eV, and B_0 in nT. For $n_{e0} = 0.1$ cm^{-3}, $T_{e0} = 400$ eV, and $B_0 \sim 3.2$ nT, we obtain $B_{\mathrm{D}} \sim 1.2$ nT.

Equation (4) expresses the magnetic-field strength outside the current layer produced by the diamagnetic current. The magnetic field produced by the diamagnetic current at an altitude H in the current layer is derived by adding the magnetic field produced by the currents above and below H,

$$B_{\mathrm{D}}(H) = -\int_0^H \frac{\mu_0 J_e(H')}{2}\mathrm{d}H' + \int_H^\infty \frac{\mu_0 J_e(H')}{2}\mathrm{d}H'. \quad (5)$$

The black line in the bottom right-hand panel of Figure 13 shows the magnetic-field intensity for each altitude, derived as $B_0 + B_{\mathrm{D}}(H)$. We perform the integration over an interval of $[H,\ 150]$ km instead of $[H,\ \infty]$ in the second term of Equation (5), since J_e above 150 km is much smaller than that below 150 km. As expected from Equation (4), $B \sim 2.0$ nT above 100 km and $B \sim 4.5$ nT near the lunar surface in Figure 13. In the current layer (0–100 km), the magnetic-field intensity increases gradually as H decreases.

Once this magnetic configuration is constructed, the electron motion and the forbidden regions in the electron VDFs are modified by the nonuniform magnetic field. We perform two-dimensional particle-trace calculations in the presence of a nonuniform magnetic field, linearly interpolated from $B_0+B_{\mathrm{D}}(H)$, as indicated by the black line in the bottom right-hand panel of Figure 13. We derived the forbidden regions for each altitude step. When we launch electrons from lower altitudes, we need more accuracy for the trajectory calculation to derive the correct forbidden regions. We trace electrons until they either strike the lunar surface or gyrate one cycle, with a time step of $T_{\mathrm{ce}}/50$ if $H > 16$ km and $T_{\mathrm{ce}}/(800/H)$ if $H \leq 16$ km. After derivation of the forbidden regions, we calculate the moments of the electron VDF once again. We then obtain a new magnetic-field distribution by integrating Equation (5). The red lines in Figure 13 show the results, iterated four times using this method. These results converge in this case as the calculation is iterated.

The magnetic-field distribution derived above can be applied to the 3D particle-trace calculation as long as the approximation of a plane lunar surface is valid; i.e., $H \ll R_{\mathrm{M}}$. The blue lines in Figure 14 show the forbidden regions derived from the 3D particle-trace calculation in the presence of a nonuniform magnetic field produced by the electron diamagnetic current. We assume that the magnetic-field intensity distribution depends on H, which we derive by iterating four times (as indicated by the red lines in Figure 13). We trace electrons until they either strike the lunar surface or gyrate one cycle, adopting a time step of $T_{\mathrm{ce}}/50$. In this case, $B \sim 2.0$ nT at 100 km and the magnetic field is enhanced as H decreases. Some of the electrons are magnetically deflected before they strike the lunar surface, resulting in smaller forbidden regions than for a uniform magnetic field. As expected from Equations (3) and (4), our calculation results of the modified forbidden regions including this diamagnetic-current effect depend on the ambient electron density, temperature, and magnetic-field strength.

We assumed that loss of hot electrons with large gyroradii, hence with large $v_\perp$, is compensated by cold electrons with $v_\perp = 0$, and therefore, $n_{ec} k_{\mathrm{B}} T_{ec\perp} = 0$. If hot electrons with $v_\perp \neq 0$ intrude along the field line, they will contribute to the electron perpendicular pressure. However, they have smaller $v_\perp$ than those of the lost electrons because the gyroradii of the intruding electrons must be smaller than the critical gyroradius, otherwise they will strike the lunar surface before they reach the loss region. Since the number of these intruding electrons does not exceed that of lost electrons to satisfy the charge neutrality condition, the loss of electron perpendicular pressure cannot be completely compensated. In other words, replacement of hot electrons by 'colder' electrons (not necessarily $n_{ec} k_{\mathrm{B}} T_{ec\perp} = 0$) results in loss of electron perpendicular pressure. Therefore, the gradient of electron perpendicular pressure is left to some extent, and the diamagnetic current does not vanish completely by hot electron intrusion, although it might be weakened compared to our calculation. We also have to be aware that our estimation of the magnetic-field variations produced by the diamagnetic-current layer might be overestimated, because we do not consider the spherical lunar surface in our calculation of the current distribution.

5. Lunar Surface-Charging Effect

If the lunar surface is charged negatively, electrons are thought to be reflected by an electric field near the lunar surface (see Figure 1c). The electric field produced by the surface potential can be shielded within a few Debye lengths (< 1 km), which is much smaller than the electron gyroradius considered here (> 10 km) [*Farrell et al.*, 2007]. Therefore, we assume that the electrons are nonmagnetized on the scale length of the surface potential. If the electric field is assumed to be radial with respect to the Moon, from the relationship between the radial velocity component of the electrons at the lunar surface $\mathbf{v}_{\rm rad}$ and the lunar surface's electrostatic potential $U_{\rm M}$ (< 0 V), the reflection condition of the electrons is given by

$$v_{\rm rad} < \sqrt{\frac{-2eU_{\rm M}}{m_e}}. \quad (6)$$

We now derive the forbidden regions in the electron VDFs by particle-trace calculation, taking this condition into account.

The red lines in Figure 14 indicate the forbidden regions for $U_{\rm M} = -500$ V in Equation (6), and the orange lines indicate the results for $U_{\rm M} = -1000$ V. Since electrons with radial velocity components that satisfy the inequality (6) are reflected at the lunar surface, these forbidden regions are smaller than those in the absence of negative lunar-surface charging (see the white regions in Figure 14). The forbidden regions with energy of 1 keV for $U_{\mathrm{M}} = -500$ and -1000 V disappear (top left-hand panel). On the other hand, the forbidden regions with an energy of 8 keV for $U_{\mathrm{M}} = -500$ and -1000 V are not very different from those generated in the absence of negative lunar-surface charging. At higher energies and large v_{rad}, fewer electrons satisfy inequality (6). For larger lunar-surface potentials, the forbidden regions become smaller, since more electrons satisfy inequality (6).

6. Perpendicular Electric-Field Effect

If an electric field component exists perpendicularly to the magnetic field and the scale length of the region characterized by the electric field is longer than the electron gyro-diameter, electrons will drift with a $\mathbf{E} \times \mathbf{B}$ drift velocity $v_{E\times B} = E_{\perp}/B$. The forbidden regions in the electron VDFs will be modified, since the electron motion is different from that in the absence of electric fields. We perform particle-trace calculations and derive the forbidden regions, taking into account four cases; i.e., $E_y < 0$, $E_y > 0$, $E_z < 0$, and $E_z > 0$, all in the presence of uniform magnetic fields oriented along the X axis. We trace electrons until they either strike the lunar surface or gyrate twenty cycles ($t \geq -20T_{ce}$). We assume a relatively strong electric field of 5 mV/m in each case to generate obvious effects for further study.

For $E_y < 0$, electrons drift in the $+Z$ direction (towards the lunar surface) as shown in Figure 1e. In this case, the forbidden regions are indicated by the red lines in Figure 15. The top left-hand panel, for an energy of 1 keV, shows no forbidden region for

$E_y = -5$ mV/m. The other panels show that the forbidden regions are smaller than those found in the absence of an electric field and they are displaced towards the bottom in all panels. This occurs because the effective height H' in the guiding center's rest frame becomes larger than H because of the $\mathbf{E} \times \mathbf{B}$ drift and H' depends on the gyrophase of the electrons that enter the sensors [*Harada et al.*, 2010].

For $E_y > 0$, electrons drift in the $-Z$ direction (away from the lunar surface) and the forbidden regions are shown by the orange lines in Figure 15. These forbidden regions have rather different distributions from those for the other cases, especially for the lower-energy electrons. Note that the regions around pitch angles $\alpha = 90°$ correspond to the forbidden regions, for example in the top left-hand panel, the region around $60 < \alpha < 120°$ indicates the forbidden region. Figure 1f shows the trajectories of an electron outside and in the forbidden region by the light blue and purple traces, respectively (the initial angles are indicated by the circles and arrows of the same colors in the top right-hand panel of Figure 15). Electrons with pitch angles around 90° have small velocity components parallel to the magnetic field, so they drift towards the lunar surface under reverse tracking and strike the lunar surface, as shown by the purple trace. On the other hand, electrons with large velocity components parallel to the magnetic field do not strike the lunar surface, because we assume that the Moon is a sphere, as shown by the light blue trace in Figure 1f. The forbidden regions for higher energies exhibit similar distributions to those in the absence of an electric field, because the $\mathbf{E} \times \mathbf{B}$ drift becomes less effective.

For $E_z < 0$ and $E_z > 0$, the forbidden regions are indicated by the green and blue lines in Figure 15, respectively. The forbidden regions for $E_z < 0$ (indicated by the green lines) become larger and those for $E_z > 0$ (indicated by the blue lines) become smaller than those in the absence of electric fields. This can be explained as follows. If an electron enters the sensor with a velocity $\mathbf{v}_\perp = (0, v_y, v_z)$, as illustrated in Figure 1b, Equation (1) becomes

$$r_\mathrm{c} = \frac{H}{1 - \cos\psi} = \frac{H}{1 + v_y/v_\perp}, \tag{7}$$

where $v_\perp = |\mathbf{v}_\perp|$. Using this relation, the condition that the electron strike the lunar surface, $r_L \geq r_\mathrm{c}$, is converted to

$$\frac{m_e v_\perp}{eB} \geq \frac{H}{1 + v_y/v_\perp} \tag{8}$$

$$v_\perp + v_y - \frac{eBH}{m_e} \geq 0, \tag{9}$$

where m_e is the electron mass and e the elementary charge. For $E_z < 0$ and $E_z > 0$, an electron drifts into the $-Y$ and $+Y$ directions, respectively, and the velocity of the electron in the guiding center's rest frame is given by $\mathbf{v}_\perp{}' = \mathbf{v}_\perp - \mathbf{v}_{\mathbf{E}\times\mathbf{B}} = (0, v_y - E_z/B, v_z)$. Hence, inequality (9) is modified to

$$v'_\perp + v_y - \frac{E_z}{B} - \frac{eBH}{m_e} \geq 0. \tag{10}$$

Since (left-hand side [LHS] of inequality (9)) $-$ (LHS of inequality (10)) $= v'_\perp - v_\perp - E_z/B$, and using triangle inequalities, $v'_\perp + |E_z/B| \geq v_\perp$ and $v_\perp + |E_z/B| \geq v'_\perp$, we obtain the following relationships: if $E_z < 0$, (LHS of inequality (10)) $\geq$ (LHS of inequality (9)), and if $E_z > 0$, (LHS of inequality (10)) $\leq$ (LHS of inequality (9)). Therefore, for $E_z < 0$, more electrons satisfy inequality (10) and the forbidden regions become large. In contrast, fewer electrons satisfy equality (10) and the forbidden regions become small for $E_z > 0$.

Finally, we summarize the perpendicular electric-field influence on the forbidden regions in the electron VDFs caused by the gyro-loss effect. For $E_y < 0$, the forbidden regions become smaller and they shift in the $-v_z$ direction. For $E_y > 0$, the forbidden regions appear like the regions with pitch angles of approximately 90°. For $E_z < 0$, the forbidden regions become larger. For $E_z > 0$, the forbidden regions become smaller. In all cases, perpendicular electric-field effects appear less clearly in the forbidden regions for higher energies.

7. Discussion

In this section, we discuss the electrons' interaction with the lunar surface, as well as with the lunar plasma environment, by comparing the observed nongyrotropic empty regions with the forbidden regions modified by taking into account the mechanisms described in the previous sections.

During Event 1, the observed electron density and temperature were relatively low and the magnetic-field intensity was fairly strong (0.10 cm^{-3}, 88 eV, and 4.6 nT). Therefore, the diamagnetic-current effect is not significant in this case. If we assume $n_{e0} = 0.10$ cm^{-3}, $T_{e0} = 88$ eV, and $B_0 = 4.6$ nT, we obtain $B_{\mathrm{D}} \sim 0.2$ nT using Equation (4). Using these observed values as ambient-plasma parameters is, in fact, not appropriate, since Kaguya was thought to be located in the diamagnetic-current layer; using Equation (3), we estimate $L \sim 33$ km $> H = 12$ km. However, we can at least estimate the order of magnitude of the magnetic-field strength produced by the diamagnetic-current system, and this magnetic field seems to be too weak to modify the electron motion.

The red dashed lines in Figure 4 indicate the modified forbidden regions for $U_{\mathrm{M}} = -50$ V in Equation (6). The forbidden regions become small, because some of the electrons are reflected due to the lunar surface's electrostatic potential. The red dashed lines seem to correspond to the inner edges of the observed empty regions, suggesting that the electrons in the regions between the red solid and dashed lines were reflected because of lunar-surface charging. The surface potential of -50 V is quite reasonable compared with the observed electron temperature of 88 eV and previous Lunar Prospector observations, which show potentials of -150 to 0 V in the magnetotail lobes [*Halekas et al.*, 2008]. In addition, although we cannot observe an upward-going electron beam from the lunar surface during Event 1 (because the magnetic-field line passing through the spacecraft was not connected to the Moon), electron beams with energies of ~ 50 eV were observed by Kaguya just before and after the time interval of Event 1 as shown by the black arrows in Figure 5. Therefore, despite the fact that we cannot completely exclude the possibilities of perpendicular electric-field and magnetic-anomalies-related effects, lunar-surface charging is thought to be the most plausible mechanism to produce the slight differences between the observed empty and forbidden regions which assume a uniform magnetic field and the absence of any electric field.

The Moon was located in the solar wind during Event 2, and lunar-surface charging would not contribute significantly, because Kaguya was located on the dayside of the Moon (solar zenith angle 39°), where the lunar surface is usually charged positively [*Halekas et al.*, 2008]. When Kaguya is located above the current layer or near its top edge, most electrons are not lost, except for higher-energy electrons, as shown in Figure 13. Therefore, we can use the observed density and electron temperature as approximations of the ambient-plasma parameters to estimate the diamagnetic-current effect as described in Section 4. During Event 2, Kaguya was thought to be located above the current layer.

If we assume $n_{e0} = 3.20$ cm^{-3}, $T_{e0} = 21$ eV, and $B_0 = 6.2$ nT, we obtain $L \sim 12$ km from Equation (3) and $B_\mathrm{D} \sim 1.1$ nT from Equation (4). Therefore, $B \sim 5.1$ nT at $H = 14$ km, which is consistent with the observed magnetic-field intensity. The modified forbidden regions in the presence of the diamagnetic-current effect are indicated by the orange lines in Figure 6. In addition, we can estimate the perpendicular electric-field effect by deriving the solar-wind convection electric field $\mathbf{E} = -\mathbf{V} \times \mathbf{B}$ from the data obtained by IEA and LMAG. The yellow lines in Figure 6 indicate the modified forbidden regions, taking into account the solar-wind convection electric-field effect, while the green lines indicate the forbidden regions when both the diamagnetic-current and the perpendicular electric-field effects operate. The green lines seem to be somewhat smaller than the observed empty regions, suggesting that one or both of these effects might be slightly overestimated. In any case, the orange and yellow lines are in general agreement with the observed empty regions, indicating that the gyro-loss effect can be affected by nonuniform magnetic fields caused by the diamagnetic-current system and/or the electron-drift motion due to the solar-wind convection electric field.

During Event 3, the Moon was located in the central plasma sheet and Kaguya was thought to be located near the top edge of the diamagnetic-current layer. If we assume $n_{e0} = 0.06$ cm^{-3}, $T_{e0} = 446$ eV, and $B_0 = 3.0$ nT, we obtain $L \sim 113$ km from Equation (3) and $B_\mathrm{D} \sim 0.9$ nT from Equation (4), resulting in $B \sim 2.1$ nT at $H = 109$ km. Using the observed density and electron temperature as ambient-plasma parameters, the modified forbidden regions in the presence of the diamagnetic-current effect are derived as indicated by the orange solid lines in Figure 8. Although the diamagnetic-current effect works substantially because of the relatively high electron temperature and the weak magnetic field, this effect does not seem to be sufficient to account for the electrons observed in the forbidden regions. From the data obtained by IEA and LMAG during Event 3, the convection electric field of the Earth's magnetosphere is estimated to be lower than 1.0 mV/m, which can hardly modify the forbidden regions with energies greater than a few keV (not shown in Figure 8 because they almost coincide with the orange lines).

When the Moon is located in the terrestrial plasma sheet, it is known that the lunar-surface potentials can be up to ~ -1000 V [*Halekas et al.*, 2008]. The modified forbidden regions that take into account the lunar surface-charging effect for $U_{\mathrm{M}} = -1000$ V in addition to the diamagnetic-current effect are indicated by the orange dashed lines in Figure 8, which roughly correspond to the observed empty regions. A small fraction of the electron population is still found in the modified forbidden regions, but it seems that the diamagnetic-current effect and lunar-surface charging are the predominant mechanisms responsible for modifying the forbidden regions during Event 3.

Event 4, shown in Figure 9, was also analyzed in our previous work. It suggests the presence of a relatively strong electric field of 10 mV/m [*Harada et al.*, 2010]. However, our previous work considered neither the diamagnetic-current effect nor lunar-surface charging. During Event 4, Kaguya was thought to be located near the top edge of the diamagnetic-current layer. If we assume $n_{e0} = 0.07$ cm^{-3}, $T_{e0} = 435$ eV, and $B_0 = 3.1$ nT, we obtain $L \sim 107$ km from Equation (3) and $B_{\mathrm{D}} \sim 1.0$ nT from Equation (4). The orange solid lines in Figure 9 indicate the modified forbidden regions, taking into account the diamagnetic-current effect using these values as ambient-plasma parameters, and the orange dashed lines indicate the forbidden regions in the presence of the diamagnetic-current effect and a lunar-surface potential of -1000 V. These modified forbidden regions under the influence of the diamagnetic-current effect and lunar-surface charging do not seem to be in agreement with the observed empty regions, especially not in the regions with positive elevation angles.

Finally, we take into account the perpendicular electric-field effect during Event 4. The estimated convection electric field of the Earth's magnetosphere (less than 0.9 mV/m) can hardly modify the forbidden regions with energies of a few keV. However, an electric field can become locally stronger than the convection electric field if the scale length of the region characterized by the strong electric field is shorter than the ion gyrodiameter, as discussed by *Harada et al.* [2010]. The yellow solid lines in Figure 9 indicate the modified forbidden regions under a perpendicular electric field of 5 mV/m and the diamagnetic-current effect, while the yellow dashed lines indicate those where we additionally assumed a surface potential of −1000 V. We assume an electric field corresponding to $E_y < 0$ in Section 6, because the forbidden regions with positive elevation angles become smallest in this case. The yellow lines seem to be more consistent with the observed empty regions than the orange lines, suggesting that an electric field of at least 5 mV/m, i.e., half as strong as that inferred by *Harada et al.* [2010], is needed to explain this event by the mechanisms discussed in this paper. Even if this electric field exists, the mechanism responsible for the production of such a strong electric field is unknown at the present.

The electron gyro-loss events observed in the Earth's magnetosphere and the solar wind have been analyzed in this section by considering the three mechanisms that modify the forbidden regions in the electron VDFs. Each event shows that the characteristics of the nongyrotropic electron VDFs associated with the gyro-loss effect depend significantly on the ambient plasma and the lunar-surface conditions. We selected the events observed near the weak and/or small-scale crustal-field regions in this paper, but if nonuniform magnetic fields related to lunar magnetic anomalies are taken into account, the process responsible for producing nongyrotropic electron VDFs will be even more complicated. Further investigation into the gyro-loss effect near lunar magnetic anomalies is needed. In any case, variations in the plasma environment near the Moon lead to various nongyrotropic electron VDFs near the lunar surface.

Kaguya's low orbital altitudes of less than the electron gyrodiameter and the excellent angular resolutions of ESA-S1 and ESA-S2 enable clear detection of nongyrotropic electron VDFs. We now know that nongyrotropic electrons commonly exist near the lunar surface and that spacecrafts orbiting at lower altitudes than $\sim$100 km are able to detect them. The vicinity of the lunar surface would be one of the suitable environments for investigation of nongyrotropic electrons, including their wave–particle interactions, which have rarely been studied observationally because of the difficulty of detecting nongyrotropic electron VDFs.

Nongyrotropic electrons near the lunar surface might have implications for surface electrostatic potentials and dust dynamics. *Reiff and Burke* [1976b] mentioned the effect of magnetic shadowing on lunar surface potentials. Shadowing of the incoming flux depending on the ambient magnetic field direction as well as photoelectrons returned to the surface by crustal magnetic fields could alter the incident currents to the surface, and therefore, the equilibrium surface potential. In addition to shadowing effect on the total incident flux to a smooth surface, surface topography might be important to local potential distribution. *Farrell et al.* [2007] suggested that topographic features such as mountains or crater rims could create local sunlit/shadow regions and local plasma void, leading to the formation of local electric fields and the acceleration of charged dust grains. Highly angular-dependent hot electrons could also influence the surface potential distribution according to the surface topography, causing local electric fields and charged dust motion. This effect would be significant especially in the plasma sheet, where large incident flux of hot electrons is expected.

While the loss of hot electrons in the plasma sheet including its angular dependence was observed on the lunar surface [*Reiff and Burke*, 1976b], magnetic-field variations associated with the diamagnetic-current layer near the lunar surface have not been reported thus far. Even if indeed the near-surface current layer exists, there seems to be some difficulty to find the clear signatures of the diamagnetic-current-related fields. As *Reiff* [1976a] mentioned, magnetic shadowing occurs infrequently at the Apollo sites located at relatively low latitudes and low longitudes, because magnetic fields in the Earth's magnetosphere at lunar distance are typically B_x-dominant and they rarely become parallel to the lunar surface there. In the solar wind, on the other hand, the interaction of crustal magnetic fields with the solar-wind plasma would be predominantly observed on the surface [*Dyal et al.*, 1972].

Single spacecraft measurement cannot distinguish the ambient field $\mathbf{B}_0$ and the diamagnetic-current field $\mathbf{B}_\mathrm{D}$. In order to detect $\mathbf{B}_\mathrm{D}$ by a spacecraft, the spacecraft needs to move along the gradient of perpendicular pressure (across the current layer) faster than $\mathbf{B}_0$ changes. Such a trajectory seems to be not so easy for the electron-perpendicular-pressure gradient near the lunar surface, since the spacecraft needs to sweep the altitudinal structure faster than $\mathbf{B}_0$ changes. In contrast, it is quite possible for the pressure gradient across the wake boundary, where various spacecrafts have observed diamagnetic-current-related fields. It seems possible to find the signatures of $\mathbf{B}_\mathrm{D}$ near the lunar surface using two spacecrafts, but very careful investigation would be needed in order to identify $\mathbf{B}_\mathrm{D}$, because the ambient magnetic field is frequently turbulent in the plasma sheet or in the solar wind.

It would be a real challenge to understand the current systems near the Moon comprehensively, including the diamagnetic current layer near the lunar surface. If the diamagnetic current actually exists near the lunar surface, it might be connected to the diamagnetic current system near the wake boundary in the solar wind, and perhaps to some kind of currents associated with magnetic anomalies, which might form a miniature magnetosphere [*Lin et al.*, 1998]. Further analysis of data obtained by recent spacecrafts such as Kaguya or ARTEMIS, as well as careful reanalysis of data in the Apollo era, will be necessary to understand the lunar plasma environment from the viewpoint of current systems.

The gyro-loss effect is a fundamental process associated with charged and magnetized particles and boundaries. This effect will be distinctly observed, particularly around sharp boundaries such as provided by solid surfaces. Various components can affect the production of nongyrotropic VDFs. In other words, analysis of nongyrotropic VDFs might provide a wealth of information on plasma environments near surfaces. The basic process can be applied to other airless bodies such as Mercury, asteroids, other moons, and distant comets.

8. Conclusion

Nongyrotropic electron VDFs observed near the lunar surface (at altitudes of ∼10–100 km) by Kaguya have been analyzed and compared with theoretical predictions from particle-trace calculations. Nongyrotropic empty regions in the electron VDFs are produced by the gyro-loss effect, which is attributed to the absorption of electrons by the lunar surface, combined with electron gyromotion. Based on particle-trace calculations, we derived theoretical forbidden regions in the electron VDFs and considered the modifications to the forbidden regions caused by nonuniform magnetic fields associated with diamagnetic-current systems, lunar-surface charging, and electric fields oriented perpendicular to the magnetic field.

The nongyrotropic electron VDF caused by the gyro-loss effect corresponds to a diamagnetic current seen in the electron VDF. The diamagnetic-current system is set up by the pressure gradient near the lunar surface and produces nonuniform magnetic-field configurations. By modeling nongyrotropic electron VDFs for different altitudes, one-dimensional distributions of the magnetic-field intensity are derived, and the modifications to the forbidden regions are estimated. The diamagnetic-current effect on the forbidden regions depends on the ambient electron density, temperature, and magnetic-field strength.

Taking surface potentials into account in the particle-trace calculations, the lunar surface-charging effect on the nongyrotropic forbidden regions is estimated. Negative surface potentials reflect the electrons and reduce the forbidden regions, depending on the electron energy. Also, calculations including the $\mathbf{E} \times \mathbf{B}$ drift term indicate that electric fields perpendicular to the magnetic fields modify the forbidden regions depending on the drift direction.

Comparison between the observed empty regions and the calculated forbidden regions suggests that various factors affect the characteristics of the nongyrotropic electron VDFs, depending on the ambient-plasma conditions. In the magnetotail lobes with low density and temperature in relatively strong magnetic fields, the diamagnetic-current effect cannot work well. Perpendicular electric fields also seem to be less effective, because plasma flows are expected to be moderate in the tail lobes. Instead, on the lunar nightside, the lunar-surface potentials slightly modify the forbidden regions. On the dayside of the Moon in the solar wind, there will be no lunar surface-charging effect on the forbidden regions with positive surface potentials, and observations suggest a solar-wind convection electric-field effect and/or a diamagnetic-current effect in relatively weak magnetic-field conditions for high densities compared with those in the Earth's magnetosphere. In the terrestrial plasma sheet, all three mechanisms can modify the forbidden regions significantly. High electron temperature and weak magnetic fields result in a strong diamagnetic-current effect despite the relatively low density. Large surface potentials in the plasma sheet will reflect higher-energy electrons. Although convection electric fields do not seem to be able to modify electron trajectories for energies of a few keV, as analyzed in this paper, they will affect lower-energy electrons that are lost at lower altitudes. One of the observations implies the presence of a local electric field of at least 5 mV/m, but the mechanism for producing this electric field is unknown.

Although we do not deal with magnetic-anomalies-related effects in this paper, further analysis of nongyrotropic electron VDFs near lunar magnetic anomalies may reveal new aspects of plasma interactions with crustal magnetic fields. In addition, nongyrotropic VDFs related to the gyro-loss effect will not only appear near the lunar surface. Charged and magnetized particles near solid surfaces will reveal clear nongyrotropic signatures. High-angular-resolution observations of nongyrotropic VDFs near solid surfaces can promote a better understanding of the near-surface plasma environment and of plasma–solid-surface interactions.

Acknowledgments. The authors express their sincere thanks to the MAP-PACE and MAP-LMAG team members for their great support in processing and analyzing the MAP data. The authors also express their gratitude to the system members of the SELENE project. This work was supported in part by a Research Fellowship for Young Scientists awarded by the Japan Society for the Promotion of Science.

References

Anderson, K. A. (1970), Method to determine sense and magnitude of electric field from lunar particle shadows, *J. Geophys. Res.*, *75*, 2591–2594, doi:10.1029/JA075i013p02591.

Anderson, K. A., R. P. Lin, C. Gurgiolo, G. K. Parks, D. W. Potter, S. Werden, and H. Rème (1985), A component of nongyrotropic (phase-bunched) electrons upstream from the Earth's bow shock, *J. Geophys. Res.*, *90*(NA11), 10,809–10,814, doi:10.1029/JA090iA11p10809.

Armstrong, T. P., T. H. Choo, E. C. Roelof, G. M. Simnett, and E. T. Sarris (1992), The effect of the shock of 15:43 UT March 23, 1991 on 50 keV to 5 MeV ions at Ulysses, *Geophys. Res. Lett.*, *19*(12), 1247–1250, doi:10.1029/92GL00777.

Coates, A. J., and G. H. Jones (2009), Plasma environment of Jupiter family comets, *Planet. Space Sci.*, *57*(10, Sp. Iss. SI), 1175–1191, doi:10.1016/j.pss.2009.04.009.

Colburn, D. S., R. G. Currie, J. D. Mihalov, and C. P. Sonett (1967), Diamagnetic solar-wind cavity discovered behind Moon, *Science*, *158*, 1040–1042, doi:10.1126/science.158.3804.1040.

Dyal, P., C. W. Parkin, C. W. Snyder, and D. R. Clay (1972), Measurements of lunar magnetic field interaction with the solar wind, *Nature*, *236*(5347), 381–385.

Farrell, W. M., T. J. Stubbs, R. R. Vondrak, G. T. Delory, and J. S. Halekas (2007), Complex electric rields near the lunar terminator: The near-surface wake and accelerated dust, *Geophys. Res. Lett.*, *34*, L14201, doi:10.1029/2007GL029312.

Futaana, Y., S. Machida, Y. Saito, A. Matsuoka, and H. Hayakawa (2003), Moon-related nonthermal ions observed by Nozomi: Species, sources, and generation mechanisms, *J. Geophys. Res.*, *108*, 1025, doi:10.1029/2002JA009366.

Gurgiolo, C., D. Larson, R. P. Lin, and H. K. Wong (2000), A gyrophase-bunched electron signature upstream of the Earth's bow shock, *Geophys. Res. Lett.*, *27*, 3153–3156, doi:10.1029/2000GL000065.

Halekas, J. S., D. L. Mitchell, R. P. Lin, L. L. Hood, M. H. Acuña, and A. B. Binder (2002), Evidence for negative charging of the lunar surface in shadow, *Geophys. Res. Lett.*, *29*, 1435, doi:10.1029/2001GL014428.

Halekas, J. S., G. T. Delory, R. P. Lin, T. J. Stubbs, and W. M. Farrell (2008), Lunar Prospector observations of the electrostatic potential of the lunar surface and its response to incident currents, *J. Geophys. Res.*, *113*, A09102, doi:10.1029/2008JA013194.

Halekas, J. S., G. T. Delory, R. P. Lin, T. J. Stubbs, and W. M. Farrell (2009a), Lunar Prospector measurements of secondary electron emission from lunar regolith, *Planet. Space Sci.*, *57*, 78–82, doi:10.1016/j.pss.2008.11.009.

Halekas, J. S., G. T. Delory, R. P. Lin, T. J. Stubbs, and W. M. Farrell (2009b), Lunar surface charging during solar energetic particle events: Measurement and prediction, *J. Geophys. Res.*, *114*, A05110, doi:10.1029/2009JA014113.

Harada, Y., et al. (2010), Interaction between terrestrial plasma sheet electrons and the lunar surface: SELENE (Kaguya) Observations, *Geophys. Res. Lett.*, *37*, L19202, doi: 10.1029/2010GL044574.

Leubner, M. (2003), An analytical representation of non-gyrotropic distributions and related space applications, *Planet. Space Sci.*, *51*(12), 723–729, doi:10.1016/S0032-0633(03)00109-0.

Lyon, E. F., H. S. Bridge, and J. H. Binsack (1967), Explorer 35 plasma measurements in the vicinity of the Moon, *J. Geophys. Res.*, *72*, 6113–6117, doi: 10.1029/JZ072i023p06113.

Lin, R. P., D. L. Mitchell, D. W. Curtis, K. A. Anderson, C. W. Carlson, J. McFadden, M. H. Acuña, L. L. Hood, and A. Binder (1998), Lunar surface magnetic fields and their interaction with the solar wind: Results from Lunar Prospector, *Science*, *281*, 1480 – 1484, doi:10.1126/science.281.5382.1480.

McCoy, J. E., R. P. Lin, R. E. McGuire, L. M. Chase, and K. A. Anderson (1975), Magnetotail electric fields observed from lunar orbit, *J. Geophys. Res.*, *80*, 3217–3224, doi:10.1029/JA080i022p03217.

McGuire, R. E. (1972), A theoretical treatment of lunar particle shadows, *Cosmic Electrodynamics*, *3*, 208–239.

Meziane, K., R. Lin, G. Parks, D. Larson, S. Bale, G. Mason, J. Dwyer, and R. Lepping (1999), Evidence for acceleration of ions to similar to 1 MeV by adiabatic-like reflection at the quasi-perpendicular Earth's bow shock, *Geophys. Res. Lett.*, *26*(19), 2925–2928, doi:10.1029/1999GL900603.

Mukai, T., T. Yamamoto, and S. Machida (1998), Dynamics and kinetic properties of plasmoids and flux ropes: GEOTAIL observations, *Geophys. Monogr. Ser.*, *105*, 117–137, doi:10.1029/GM105p0117.

Reiff, P. H. (1976a), Magnetic shadowing of charged particles by an extended surface, *J. Geophys. Res.*, *81*(19), 3423–3427, doi:10.1029/JA081i019p03423.

Reiff, P. H., and W. J. Burke (1976b), Interactions of the plasma sheet with the lunar surface at the apollo 14 site, *J. Geophys. Res.*, *81*(25), 4761–4764, doi:10.1029/JA081i025p04761.

Saito, Y., et al. (2008a), Solar wind proton reflection at the lunar surface: Low energy ion measurement by MAP-PACE onboard SELENE (KAGUYA), *Geophys. Res. Lett.*, *35*, L24205, doi:10.1029/2008GL036077.

Saito, Y., et al. (2008b), Low-energy charged particle measurement by MAP-PACE onboard SELENE, *Earth Planets Space*, *60*, 375–385.

Saito, Y., et al. (2010), In-flight performance and initial results of plasma energy angle and composition experiment (PACE) on SELENE (Kaguya), *Space Sci. Rev.*, *154*, 265–303, doi:10.1007/s11214-010-9647-x.

Schubert, G., and B. R. Lichtenstein (1974), Observations of Moon-plasma interactions by orbital and surface experiments, *Rev. Geophys. Space Phys.*, *12*, 592–626, doi:10.1029/RG012i004p00592.

Shimizu, H., F. Takahashi, N. Horii, A. Matsuoka, M. Matsushima, H. Shibuya, and H. Tsunakawa (2008), Ground calibration of the high-sensitivity SELENE lunar magnetometer LMAG, *Earth Planets Space*, *60*, 353–363.

Table 1. Plasma Conditions for Four Events

	Event 1	Event 2	Event 3	Event 4
Time period	2009/06/05 20:10:17-20:10:33	2009/04/17 11:57:22-11:58:42	2008/04/18 23:06:33-23:07:21	2008/01/21 15:00:23-15:01:11
Moon location at GSE coordinates	$(-58, 23, -5)R_\mathrm{E}$	$(-1, -63, -1)R_\mathrm{E}$	$(-60, 18, -4)R_\mathrm{E}$	$(-57, 12, 3)R_\mathrm{E}$
Kaguya location				
– Orbital height	12 km	14 km	109 km	98 km
– Latitude and longitude in selenographic coordinates	(76°S, 149°E)	(36°S, 104°W)	(62°N, 176°W)	(28°S, 92°W)
– Solar zenith angle	99°	39°	115°	106°
Magnetic field intensity	4.6 nT	5.1 nT	2.1 nT	2.1 nT
$(\phi_\mathrm{Bsat}, \theta_\mathrm{Bsat})$	(41°, 2°)	(268°, −2°)	(338°, −2°)	(239°, −11°)
Density	0.10 cm^{-3}	3.20 cm^{-3}	0.06 cm^{-3}	0.07 cm^{-3}
Ion temperature (IEA)	–	27 eV	1.93 keV	1.86 keV
Electron temperature	88 eV	21 eV	446 eV	435 eV
Bulk flow (IEA)	–	446 km/s	490 km/s	410 km/s

Takahashi, F., H. Shimizu, M. Matsushima, H. Shibuya, A. Matsuoka, S. Nakazawa, Y. Iijima, H. Otake, and H. Tsunakawa (2009), In-orbit calibration of the lunar magnetometer onboard SELENE (KAGUYA), *Earth Planets Space*, *61*, 1269–1274.

Tsunakawa, H., H. Shibuya, F. Takahashi, H. Shimizu, M. Matsushima, A. Matsuoka, S. Nakazawa, H. Otake, and Y. Iijima (2010), Lunar magnetic field observation and initial global mapping of lunar magnetic anomalies by MAP-LMAG onboard SELENE (Kaguya), *Space Sci. Rev.*, doi:10.1007/s11214-010-9652-0.

Tu, J., T. Mukai, M. Hoshino, Y. Saito, Y. Matsuno, T. Yamamoto, and S. Kokubun (1997), Geotail observations of ion velocity distributions with multi-beam structures in the post-plasmoid current sheet, *Geophys. Res. Lett.*, *24*(17), 2247–2250, doi:10.1029/97GL02113.

Yokota, S., et al. (2009), First direct detection of ions originating from the Moon by MAP-PACE IMA Onboard SELENE (KAGUYA), *Geophys. Res. Lett.*, *36*, L11201, doi:10.1029/2009GL038185.

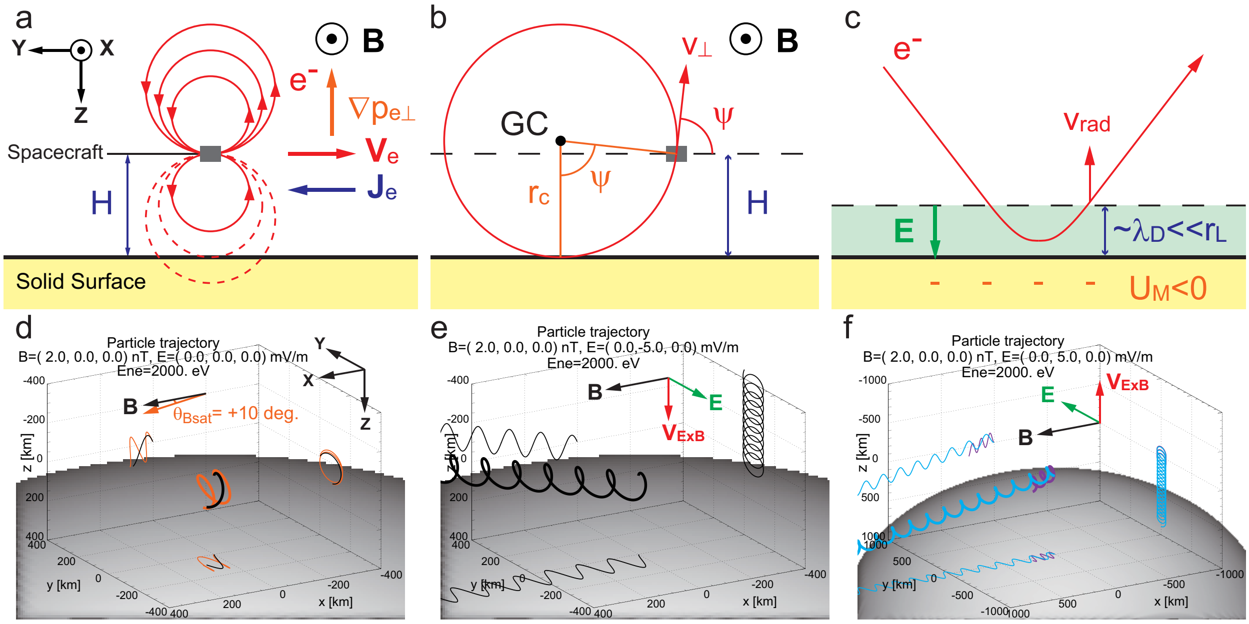

Figure 1. Schematic illustration of (a) the gyro-loss effect and the diamagnetic current, (b) the critical gyroradius, r_c, gyrophase, ψ, perpendicular velocity, $v_\perp$, spacecraft orbital height, H, and the guiding center of the electron, GC, and (c) an electron trajectory near the negatively charged lunar surface; $\mathbf{v}_{\rm rad}$ is the radial velocity component to the Moon, and the electric field $\mathbf{E}$ produced by the negative surface electrostatic potential $U_{\rm M}$ is shielded within a few Debye lengths, $\lambda_{\rm D}$, which is much smaller than the electron gyroradius, r_L. Sample electron trajectories (d) obtained from reverse tracking calculations, launched from a spacecraft altitude of 100 km with an energy of 2 keV, for a uniform magnetic field of 2 nT and no electric field; the black trace shows the trajectory for $\theta_{\rm Bsat} = 0°$ and the orange trace shows that for $\theta_{\rm Bsat} = +10°$, (e) in the presence of a uniform electric field of $E_y = -5$ mV/m and (f) for $E_y = 5$ mV/m; the light blue trace shows the trajectory launched with an initial azimuthal angle of 250° and an elevation angle of 0°, the purple trace shows the trajectory with an azimuthal angle of 260° and an elevation angle of 0°.

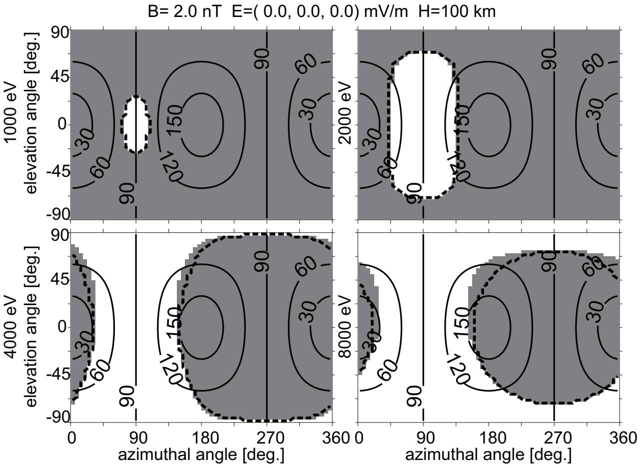

Figure 2. Forbidden regions in the electron VDF for different energies in satellite coordinates, assuming a uniform magnetic field of 2 nT in the $+X$ direction, no electric fields, and a spacecraft altitude of 100 km. The contours indicate pitch angles. The white regions show the forbidden regions derived from particle-trace calculations. The dashed lines indicate the forbidden regions derived from Equation (1).

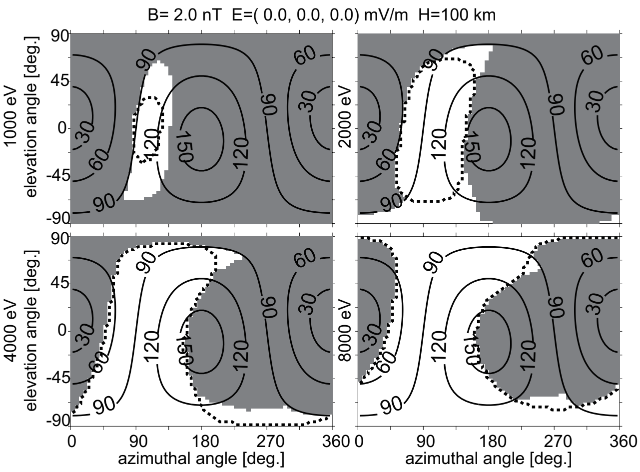

Figure 3. Forbidden regions in the electron VDF for an inclined magnetic field ($\theta_{\mathrm{Bsat}} = +10°$), in the same format as in Figure 2. The dashed lines indicate the regions where electrons strike the lunar surface during one gyrocycle.

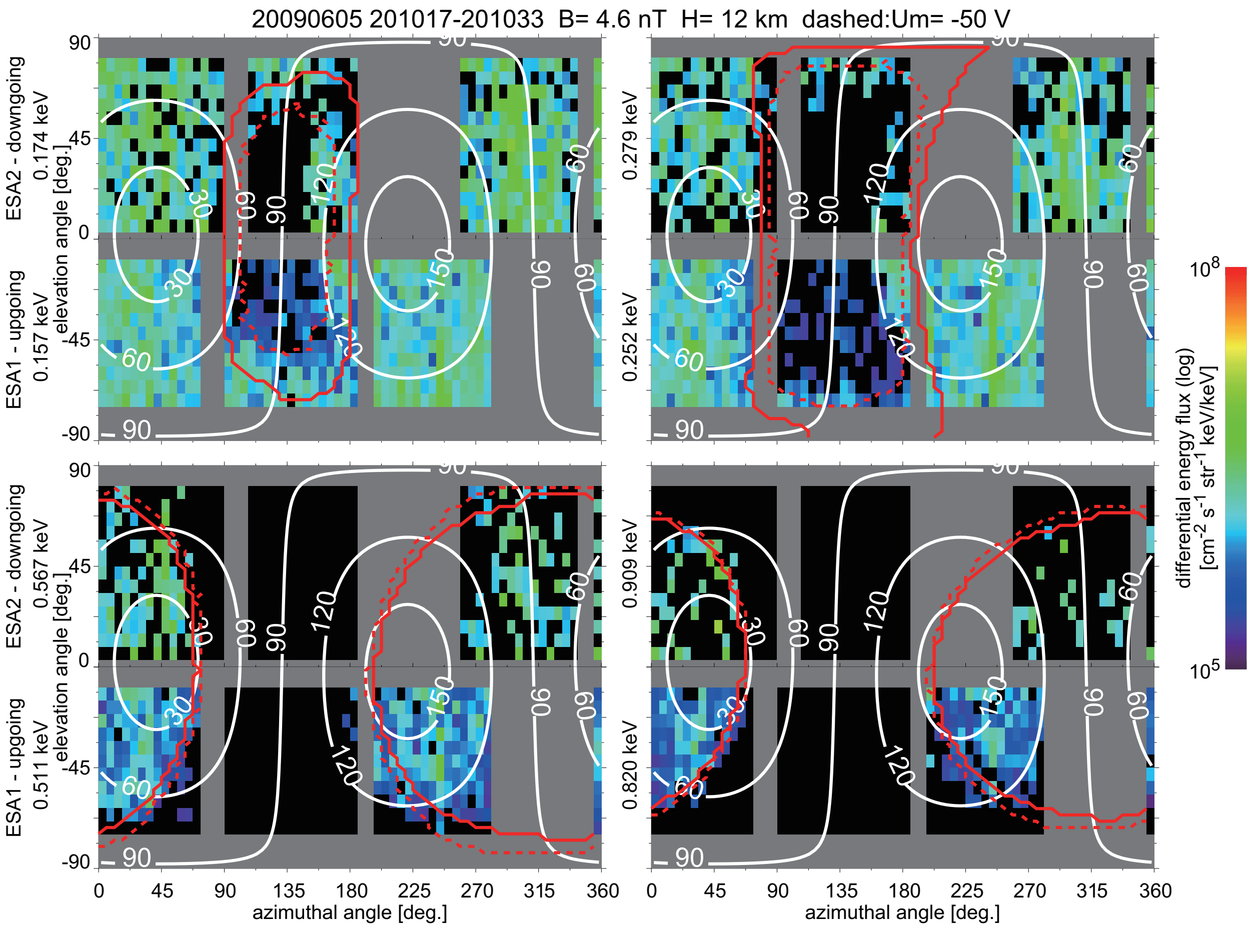

Figure 4. Electron angular distribution for different energies in satellite coordinates obtained in the period of 20:10:17–20:10:33 UT (16 s) on 5 June 2009, when the Moon was in the Earth's magnetosphere. Angles with little or no sensitivity are indicated in gray. Note that ESA-S1 and ESA-S2 have different sensitivities. The white contours represent the pitch angles. The red solid lines indicate the forbidden regions derived from particle-trace calculations for the energies of ESA-S1 and ESA-S2 shown in each panel, assuming a uniform magnetic field and no electric field. The red dashed lines indicate the modified forbidden regions for an electrostatic potential of the lunar surface of −50 V.

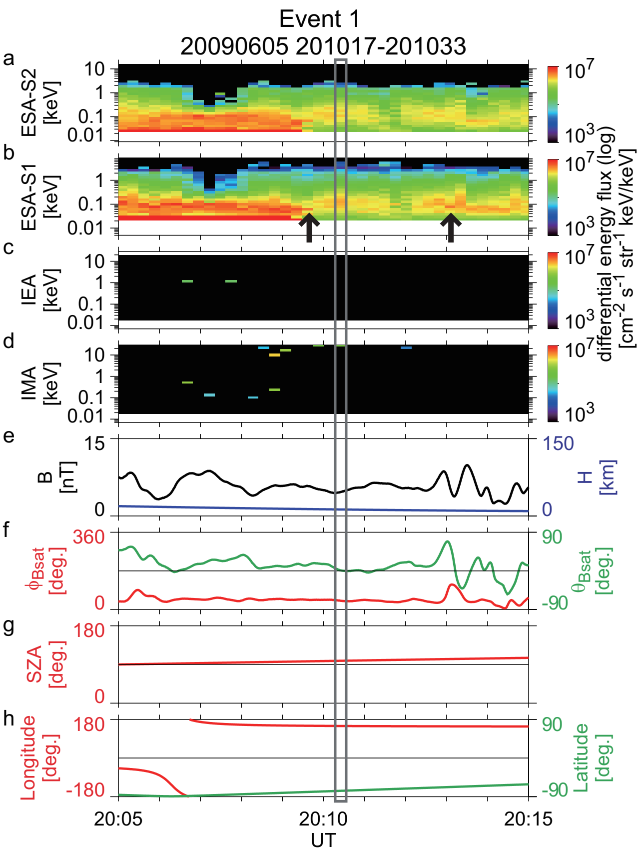

Figure 5. Time-series data from Kaguya for Event 1. (a)–(d) Energy–time spectrograms from PACE sensors, (e) magnetic-field intensity and Kaguya's orbital altitude, (f) direction of magnetic field in satellite coordinates, and (g and h) spacecraft location in solar zenith angle (SZA) and in selenographic coordinates. The gray box indicates the time period of the gyro-loss event shown in Figure 4. The black arrows in panel (b) indicate upward-going electron beams with energies of ∼50 eV, observed by ESA-S1.

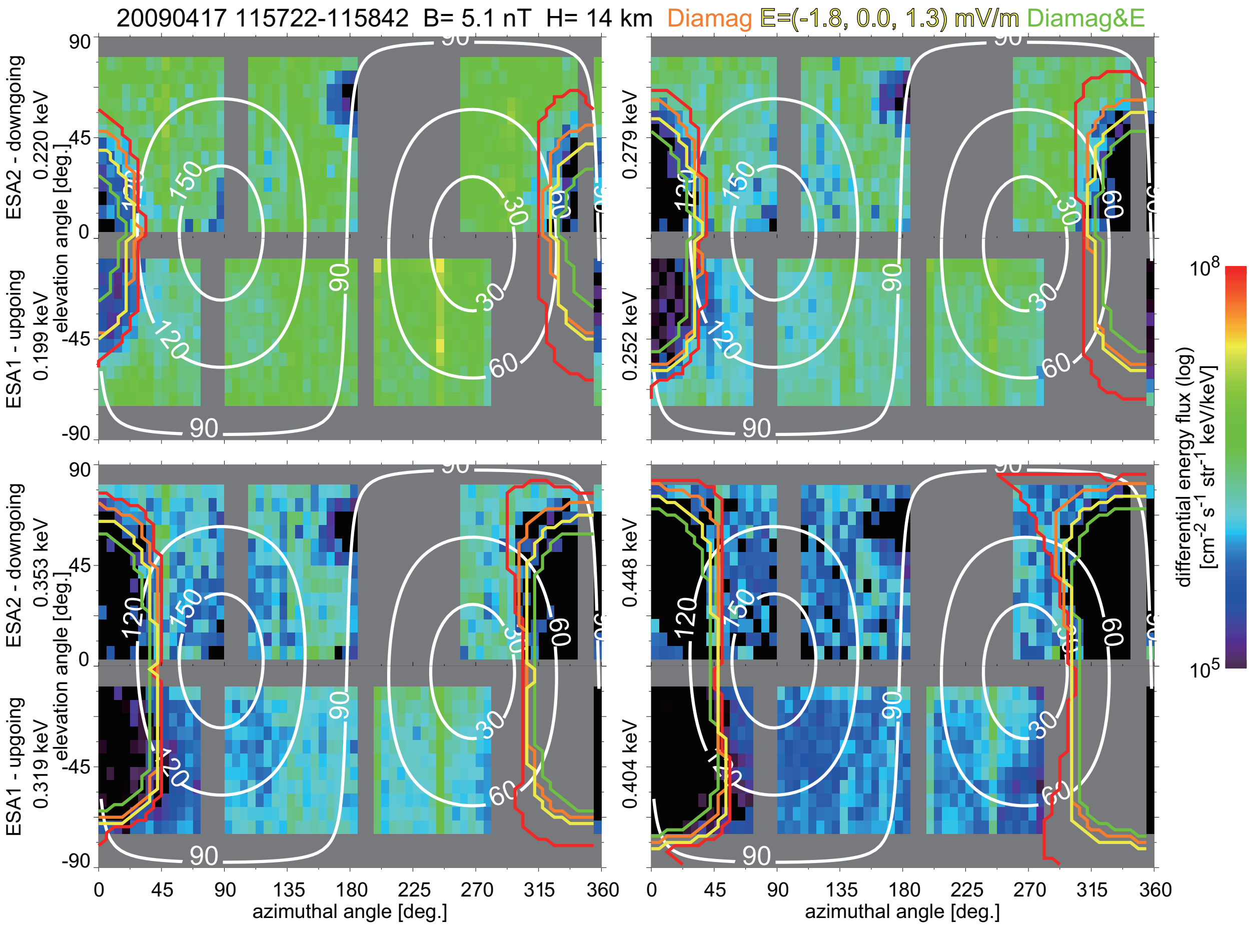

Figure 6. Electron angular distribution obtained during 11:57:22–11:58:42 UT (80 s average) on 17 April 2009, when the Moon was located in the solar wind, in the same format as in Figure 4. The red lines indicate the forbidden regions for a uniform magnetic field and no electric field. The orange lines indicate the modified forbidden regions under the diamagnetic-current effect, the yellow lines indicate those affected by a perpendicular electric field, and the green lines indicate those due to both the diamagnetic-current effect and a perpendicular electric field. A solar-wind convection electric field of 2.3 mV/m is estimated from $-\mathbf{V} \times \mathbf{B}$ using the data obtained by IEA and LMAG. The flux dips around (180°, 65°) are thought to be due to blockage of electrons by the high-gain antenna.

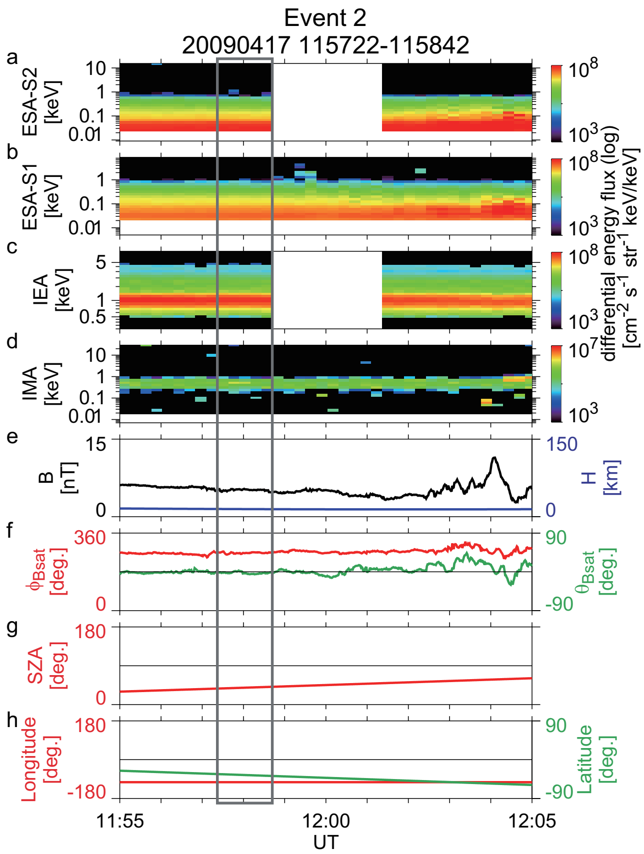

Figure 7. Time-series data from Kaguya for Event 2 in the same format as in Figure 5. The gray box indicates the time period of the gyro-loss event shown in Figure 6.

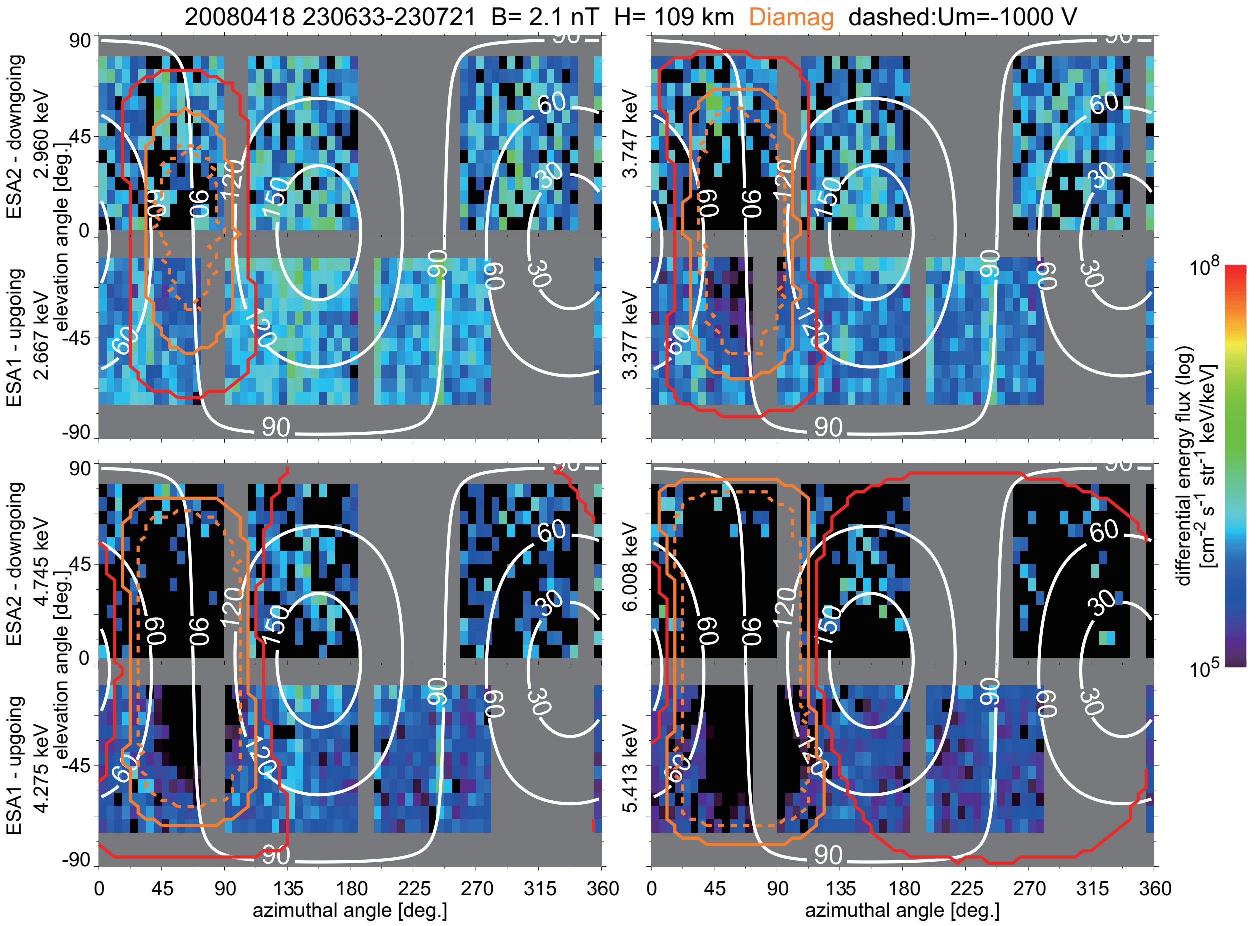

Figure 8. Electron angular distribution obtained during 23:06:33–23:07:21 UT (48 s average) on 18 April 2008, when the Moon was in the Earth's magnetosphere, in the same format as in Figure 4. The red lines indicate the forbidden regions for a uniform magnetic field and no electric field, the orange solid lines indicate the modified forbidden regions under the diamagnetic-current effect, and the orange dashed lines indicate those affected by the diamagnetic-current effect and an electrostatic potential of the lunar surface of −1000 V.

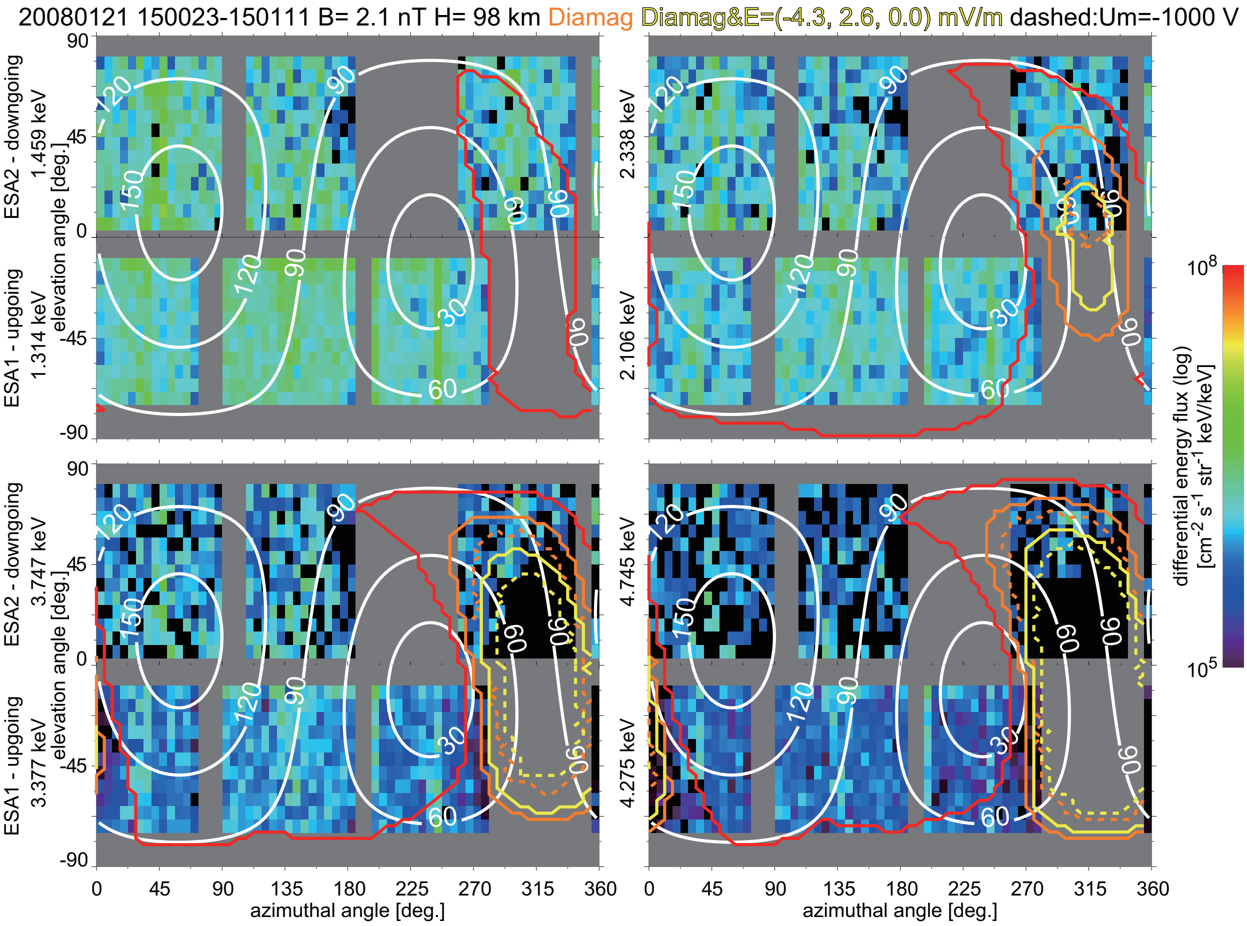

Figure 9. Electron angular distribution obtained during 15:00:23–15:01:11 UT (48 s average) on 21 January 2008, when the Moon was in the Earth's magnetosphere, in the same format as in Figure 4. The red lines indicate the forbidden regions for a uniform magnetic field and no electric field. The orange solid lines indicate the modified forbidden regions under the diamagnetic-current effect, the orange dashed lines indicate those affected by the diamagnetic-current effect and an electrostatic potential of the lunar surface of −1000 V, the yellow solid lines indicate those due to the diamagnetic-current effect and a perpendicular electric field of 5 mV/m, the yellow dashed lines indicate those under the diamagnetic-current effect, a perpendicular electric field of 5 mV/m, and a lunar-surface potential of −1000 V.

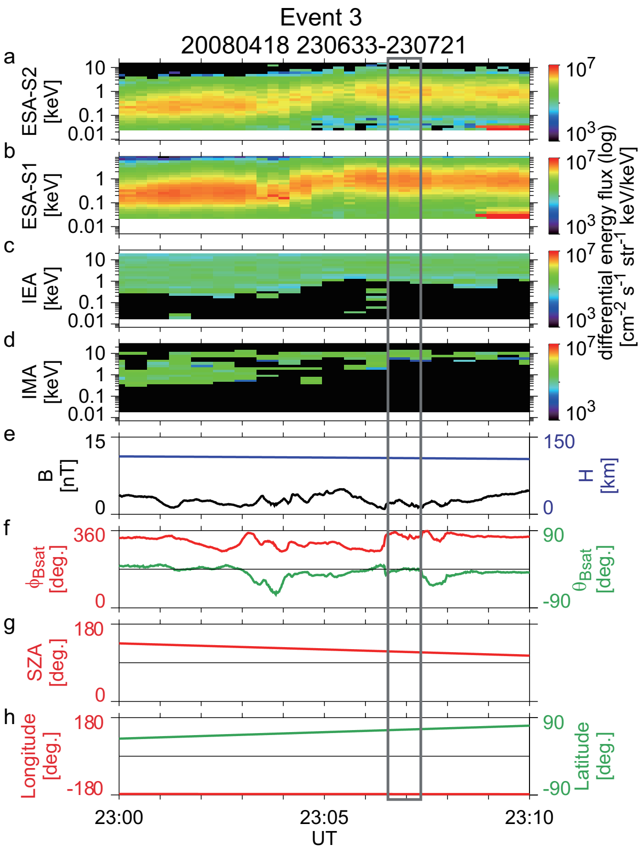

Figure 10. Time-series data from Kaguya for Event 3 in the same format as in Figure 5. The gray box indicates the time period of the gyro-loss event shown in Figure 8.

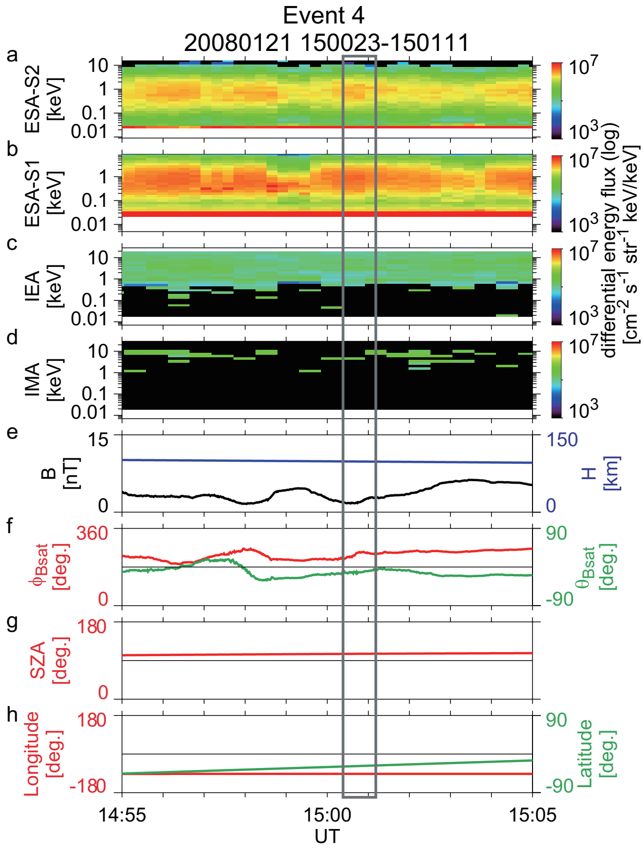

Figure 11. Time-series data from Kaguya for Event 4 in the same format as in Figure 5. The gray box indicates the time period of the gyro-loss event shown in Figure 9.

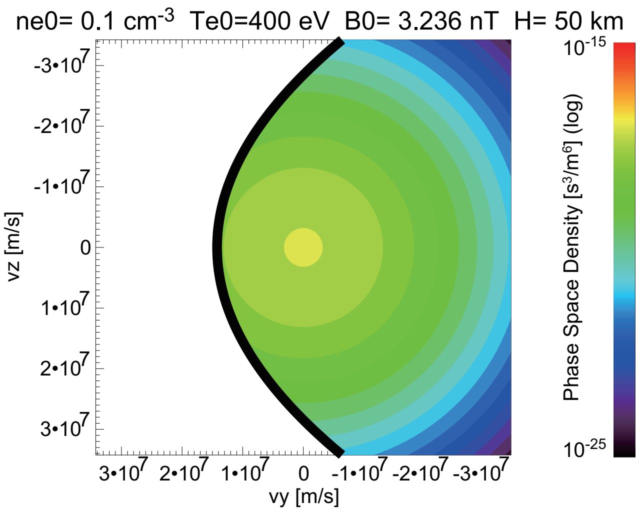

Figure 12. Cross section of the modeled electron VDF at an altitude of 50 km with an ambient magnetic field of $B = 3.236$ nT. The black line indicates the boundary of the forbidden region.

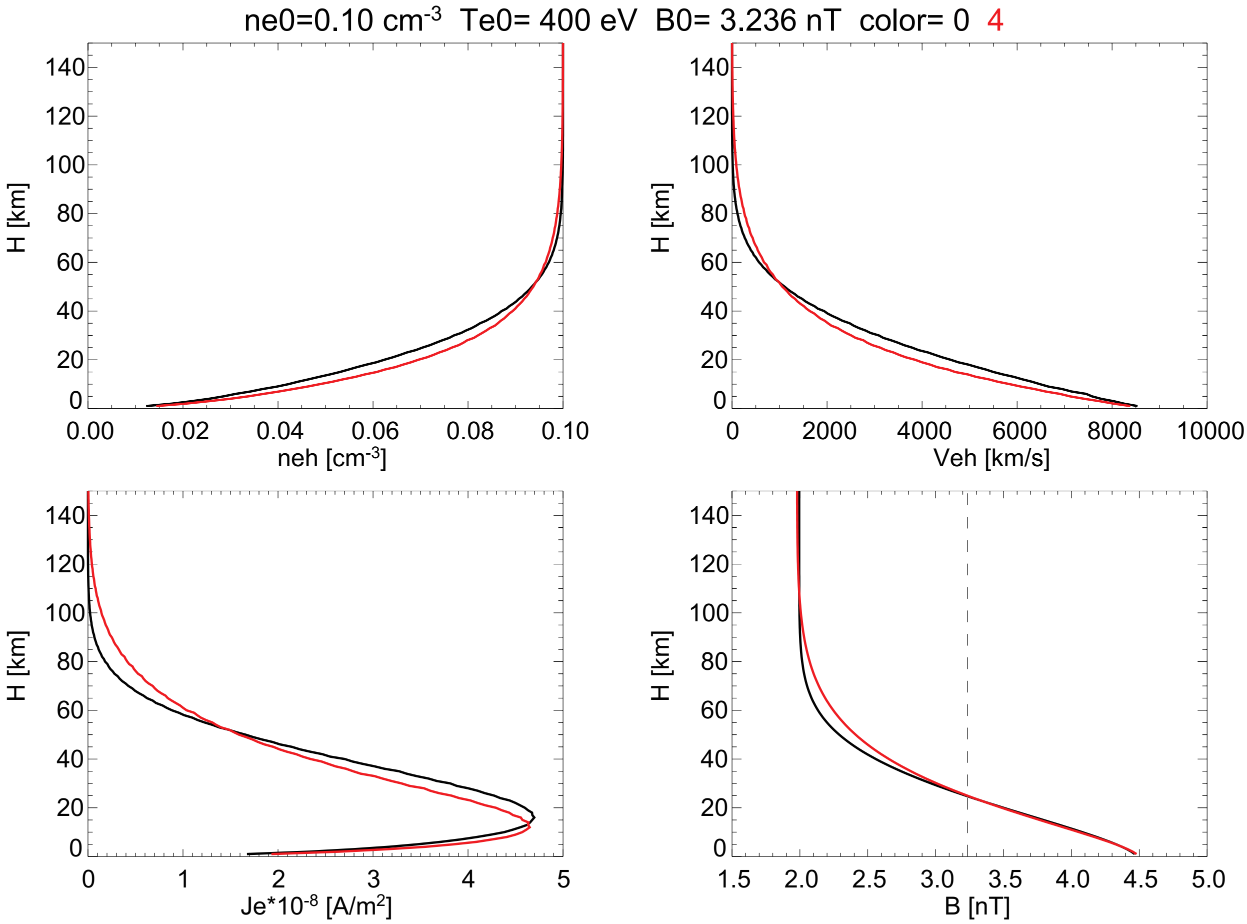

Figure 13. Calculated electron moments in the diamagnetic-current model (see text for details). Iterated results are represented by the red lines. The vertical dashed line in the bottom right-hand panel indicates the assumed ambient magnetic field strength of 3.236 nT.

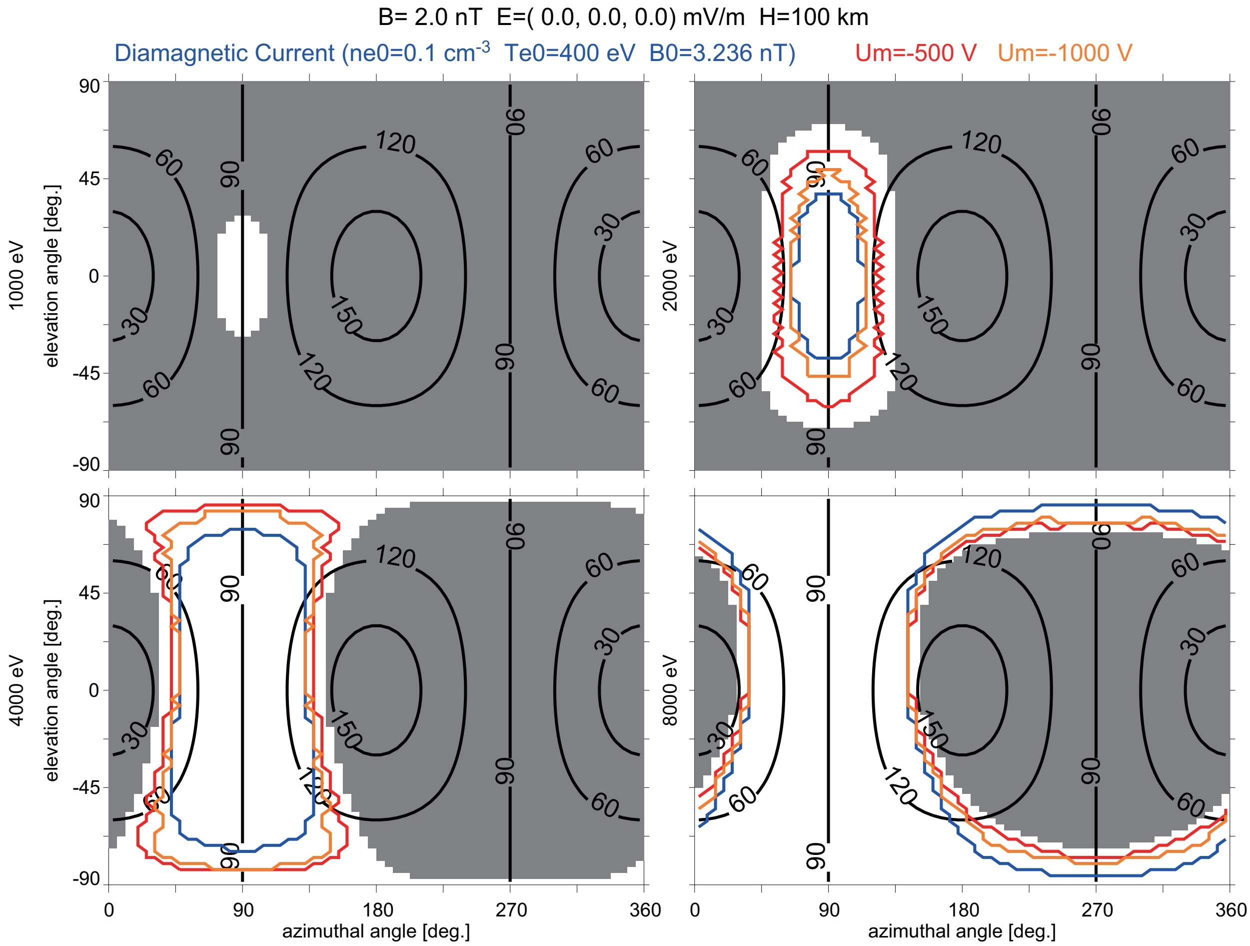

Figure 14. Forbidden regions in the electron VDF considering the diamagnetic-current effect and lunar-surface charging, in the same format as in Figure 2. The white regions indicate the same forbidden regions as in Figure 2. The blue lines indicate those taking into account the nonuniform magnetic field produced by the diamagnetic current near the lunar surface, the red lines indicate those for an electrostatic potential at the lunar surface of −500 V, and the orange lines indicate those for a surface potential of −1000 V.

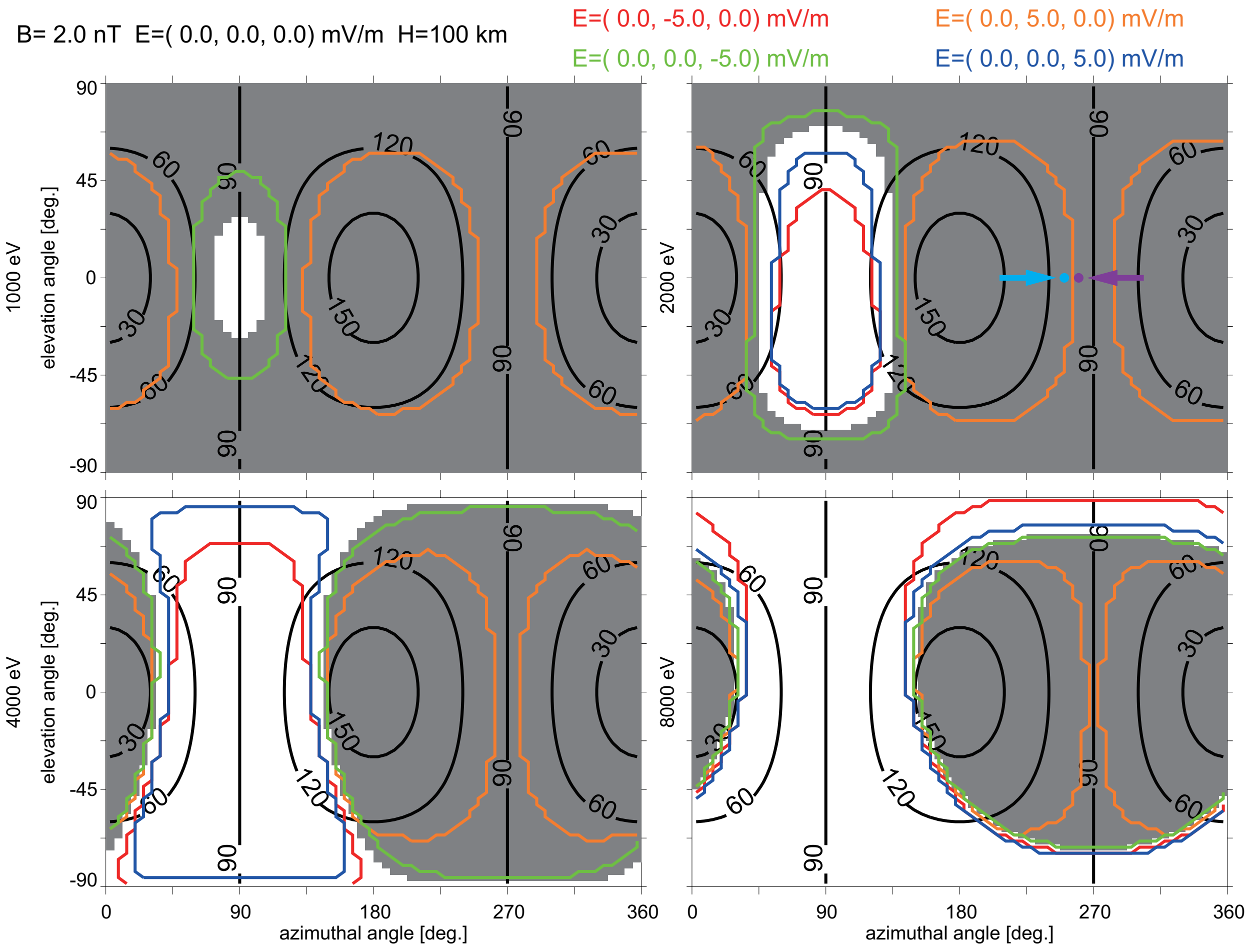

Figure 15. Forbidden regions in the electron VDF for a uniform magnetic field ($B_x = 2$ nT) and uniform electric fields perpendicular to the magnetic field, in the same format as in Figure 2. The white regions indicate the forbidden regions in the absence of electric fields. The red lines indicate those for $E_y = -5$ mV/m, the orange lines indicate those for $E_y = 5$ mV/m, the green lines indicate those for $E_z = -5$ mV/m, and the blue lines indicate those for $E_z = 5$ mV/m. The light blue circle and arrow in the top right-hand panel indicate the (250°, 0°) point, which corresponds to the light blue trajectory in Figure 1f for $E_y = 5$ mV/m, and the purple circle and arrow indicate the (260°, 0°) point, corresponding to the purple trajectory in Figure 1f.